ETH
Eidgenössische Technische Hochschule Zürich
Swiss Federal Institute of Technology Zurich

Communication Technology Laboratory
Wireless Communications Group
Prof. Dr. A. Wittneben
Sternwartstrasse 7 ETH Zentrum Zurich

Master's Thesis at the Communication Technology Laboratory
HS 2009

Ultra Wideband Location Fingerprinting: Efficient Parameter Estimation and Experimental Verification

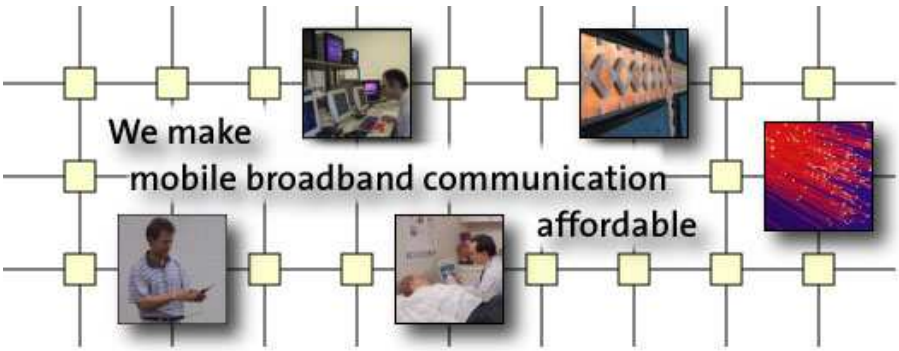

Harald Kröll

18.03.2010

Advisor: Dipl. Ing. Christoph Steiner

Professor: Prof. Dr. Klaus Witrisal

Abstract

Ultra Wideband (UWB) Location Fingerprinting is an attractive alternative to positioning concepts based on lateration or angulation. Due to the large bandwidth the channel impulse response (CIR) of a UWB transmitter is an adequate fingerprint of the relative positions of transmitter and receiver. A received CIR is related to a certain region according to the propagation properties and vice versa. The propagation environment is arranged in regions, in which a transmitting node can be located.
In the first phase, the training phase, received CIRs are assigned to the regions they are transmitted from and stored into a database. In the second phase, a received CIR from an unknown position is observed and compared to the stored CIRs. The best match indicates the region the CIR is transmitted from.
Recent publications modeled and evaluated such systems. They require an exhaustive training phase. The goal of this work is it to reduce the training effort. In the presented approach only few CIRs from a region are measured while the rest is reconstructed. The geometry of the propagation environment is taken into account in the reconstruction process. A measurement campaign in an anechoic chamber and in an office environment was performed to test the feasibility of our approach with real world measurement data.
The results were evaluated using different settings. As expected the positioning error is larger for the reconstructed CIRs than for the measured CIRs. For the office environment we obtain an average positioning error of 14 cm for the reconstructed CIRs and 10 cm for the measured CIRs with optimal settings. The region size and the amount of observations from a region are important parameters regarding the accuracy.

Keywords: Ultra Wideband, Location Fingerprinting, Positioning System, Location System, Ray Tracing, Spatial delay tracing, Channel impulse response, Hough Transform, RF Fingerprinting, office environment

Kurzfassung

Ultrabreitband (UWB) Location Fingerprinting stellt eine attraktive Alternative zu den auf Lateration und Angulation basierenden UWB Ortungsverfahren dar. Aufgrund seiner grossen Bandbreite eignet sich die Impulsantwort eines UWB Senders als Fingerabdruck der relativen Position des Senders zum Empfänger. Die Umgebung wird dabei in sog. Regionen eingeteilt auf welche sich der Aufenthaltsort des Senders beschränkt. Dies bedeutet dass aufgrund einer empfangenen Impulsantwort die Region des Senders ermittelt werden kann. In einer ersten Phase, der Trainingsphase werden empfangene Impulsantworten den Regionen zugeordnet und gespeichert. In einer zweiten Phase wird eine empfangene Impulsantwort mit den gespeicherten Impulsantworten verglichen. So kann aus der Impulsantwort die Region bestimmt werden aus welcher sie kommt und umgekehrt.
In aktuellen Veröffentlichungen wurden solche Systeme modelliert und evaluiert. Sie haben jedoch den Nachteil einer zu aufwendigen Trainingsphase. Ziel dieser Arbeit ist es den Trainingsaufwand deutlich zu verringern. Der gewählte Ansatz basiert darauf nur wenige Impulsantworten einer Region zu messen und aus diesen den Rest der Impulsantworten der Region zu rekonstruieren. Dabei wird die Interaktion der einzelnen Pfade der Impulsantwort mit der Geometrie der Umgebung in Betracht gezogen. Eine Messkampagne in einem reflexionsarmen Raum und einer Büroumgebung wurde durchgeführt um die Brauchbarkeit des gewählten Ansatzes zu ermitteln.
Die Ergebnisse der Messkampagnen wurden unter verschiedenen Gesichtspunkten ausgewertet. Wie zu erwarten war die Genauigkeit der rekonstruierten Impulsantworten unter jener der Gemessenen. Der durchschnittliche Positionierungsfehler in einer Büroumgebung bei optimalen Einstellungen beträgt 10 cm für die gemessenen und 14 cm für die rekonstruierten Impulsantworten. Die Grösse der Regionen und die Anzahl der gemessenen Impulsantworten aus einer Region stellen dabei wichtige Parameter dar.

Schüsselwörter: Ultrabreitband, Ortungssystem, Location Fingerprining, Mehrwegeausbreitung, Ultrabreitband Imaging, Büroumgebung

Contents

1 Introduction

In this chapter, we will introduce Ultra Wideband (UWB) Positioning technology and and Location Fingerprinting in general. Then we provide an overview of the latest activities in research and industry. Location Fingerprinting based on UWB channel impulse responses will be presented with the necessary mathematical models. We state the main drawback of the method and introduce suitable solutions.

1.1 UWB Positioning

Due to the large bandwidth UWB is a promising technology for positioning and ranging scenarios. The high temporal resolution of the channel impulse responses (CIRs) allows precise ranging and positioning [41].
In 2002 The FCC opened the 3.1 - 10.6 GHz band for UWB usage with a maximum EIRP level of -41.3 dBm. Since then various non-military applications based on UWB were and are appearing [26]. Most positioning systems are based on geometric techniques such as triangulation. The position of the transmitter is estimated from the distances to at least three reference receivers with known positions using ToA or TDoA measurements [20].
UWB positioning systems require low hardware complexity and low cost [21]. UWB is a technology which is able to meet those requirements as latest developments in industry and research exhibit.
Precise Real Time Location Systems (RTLS) are deployed by the companies Timedomain [18], Zebra Enterprise Solutions [6] and Ubisense [1]. Target applications include asset, person and animal tracking, supporting manufacturing processes, 3D person tracking in military training and many others.
These systems have a 3D real time accuracy up to 10-15 cm in a indoor range of 50m [26]. Some of the systems integrate other localization technologies like RFID, WiFi and GPS into one system.
In research UWB is an extensively elaborated topic since many years. Latest research trends for UWB positioning include 3D positioning with mm accuracy [42], UWB based insect motion control [8] and ultra low power concepts for wireless sensor networks [37], just to highlight a few topics.
The mentioned ultra low power designs are based on Impulse Radio (IR) UWB while the

precise 3D positioning system combines both IR and carrier based concepts [42].
The US army uses UWB radars which deliver 3D view trough walls [30]. These trough-wall radar devices called "Eagle handheld scanners" are developed by the company Tialinx [17].

1.2 Location Fingerprinting

Positioning systems based on location fingerprinting establish a relationship between a physical measurement and a specific location [21]. In many cases the received signal strength (RSS) is the physical measurement. In other words Location Fingerprinting systems assign a received signal from an unknown region to the region it comes from. A region can be thought as an area in a 2D environment. Parameters characterizing signals received from a certain position in the environment represent a signature of the transmitter position. In this way a rough localization can be performed in a two phase procedure.
First the system collects fingerprints of known training points and files them together with the coordinates of the training points into a database. Next the system observes a fingerprint from an unknown location and tries to find the best matching entry in the database [33]. This technique is also called Location Pattern Matching [21].
This method is an alternative to positioning systems based on geometric techniques such as ToA (Time of Arrival) and AoA (Angle of Arrival).
The accuracy of systems using geometric positioning techniques suffers under a rich multipath environment and non line of sight (NLOS) channels because the detection of the direct path becomes difficult [20]. UWB is an appropriate technique for dense multipath environments because in many channels of interest its time spread is much larger than its time resolution. Another advantage of location fingerprinting systems is that they require a single receiver and no time synchronization. The hardware complexity can be concentrated on a single receive station [33].
Positioning systems based on location fingerprinting are popular among 802.11 wireless networks using received signal strength (RSS) patterns as fingerprints. Examples for systems of this type are Ekahau [16] or RADAR [3]. However RSS based 802.11 location fingerprints have only one degree of freedom per access point which may result in poor accuracy by using only a few access points. A location fingerprint with more degrees of freedom increases the performance. In UWB systems it is possible to directly use the channel impulse response as fingerprint due to its large bandwidth. A UWB-CIR based location fingerprinting method is shown in [2, 33]. Also low complexity UWB location fingerprinting can be performed using the output samples of an energy detector receiver [34]. In this work CIR based UWB location fingerprinting is treated.

1.3 System Model

1.3.1 Spatio-Temporal Signal Model

The signal model used for fingerprinting investigates time and space. The received signal $y(t, x, y)$ as a superposition of delayed copies of a pulse form $s(t)$ is given in passband representation (1.1) and complex baseband representation (1.2).

$$y_c(t, x, y) = \sum_{l=1}^{L} \gamma_l(x, y) s_l^c(t - \tau_l(x, y)) + \omega^c(t) \tag{1.1}$$

$$y(t, x, y) = \sum_{l=1}^{L} \gamma_l(x, y) e^{-j2\pi f_c \tau_l(x,y)} s_l(t - \tau_l(x, y)) + \omega(t) \tag{1.2}$$

L is the number of paths, f_c the carrier frequency, $\omega^c(t)$ is AWGN, $\omega(t)$ is complex AWGN, $s_l^c(t)$ the band limited passband pulse, $\tau(x, y)$ the path delay depending from the location and $\gamma(x, y)$ are the real valued gains.
This signal model does not consider time varying gain coefficients. Even different pulse shapes for different reflections are not investigated. A UWB channel model which considers incidence azimuth and Doppler frequency is presented in [11] but due to the high estimation effort it is no suitable for our case.
An other channel model divides the propagation paths into specular-alike paths (concentrated propagation paths) and paths resulting from distributed diffuse scattering [29]. The CIRs of our investigated environments did not show distributed diffuse scattering in an amount it would have been traceable. Therefore this approach was not applicable to our system.

1.3.2 Region Modeling

Regions are areas in an environment (2D euclidean space) described by a squared grid with a certain spacing between the grid points. Each point on the grid represents a possible TX antenna location. We assume a region can emit W^2 CIRs and has a width of W.
To be able to assign received CIRs to a region we need methods to compare properties of the CIRs from a certain region with properties of the received CIR. In this case as already used in [33] a complex Gaussian probability distribution is used to describe the CIRs.
Each discrete time CIR represents an observation of a complex Gaussian random vector. Each element of the random vector is a random variable representing a channel tap. With this method our system becomes mathematically traceable [33].

The probability density of a CIR observation arising from region A is given by (1.3). The CIR is given by the discrete time observation vector $\mathbf{y} = [\ y[1] \quad \dots \quad y[N]\ ]^T$.

$$p(\mathbf{y}|A) = \mathcal{CN}(\mathbf{\Sigma}_A, \mu_A) = \pi^{-N}|\mathbf{\Sigma}_A|^{-1}\exp(-(\mathbf{y}-\mu_A)^H\mathbf{\Sigma}_A^{-1}(\mathbf{y}-\mu_A)) \tag{1.3}$$

Alternative modeling approaches use the average power delay profile as modeling parameter for each region. They are presented in [2]. In this case only the diagonal of $\mathbf{\Sigma_A}$ is used. This approach assumes independent CIR taps.

1.3.3 Problem Statement

It is shown in [33] that the covariance approach reaches better performance results as the power delay profile approach. For regions which are side by side, so called neighbor regions the performance difference between the two methods is significantly large.
A drawback of both methods is the exhaustive training phase. For each region around $0.3 \cdot W^2$ CIRs have to be measured to be able to get accurate parameter estimates for the covariance matrix and the mean vector [33]. The focus of this work lies mainly on the reduction of the training effort and its experimental verification by using a reduced amount of measurements and by doing a reconstruction of the missing CIRs.

1.3.4 Proposed Solution

The approach presented in this work takes into account the geometry of the propagation environment for a two-dimensional Euclidean space. The interactions between path delays and the geometry of the environment are investigated. Only a few observations are used to explore the spatial behavior of the path delays. The rest of the CIRs from the region grid are reconstructed from the propagation knowledge gained from the observations.
The present environment consists of a finite number of specular reflectors and point scatterers. The delays of the distracted paths are calculated analytically using common ray-tracing formulas based on Euclidean geometry.

Point Scatterer

Each point scatterer l is defined by its coordinates $(x_d, y_d)_l$. A scattered path delay can be expressed as in (1.4), where $a = -x_d$ and $b = -y_d$.

$$\tau(x,y) = \frac{1}{c_0}\left(\sqrt{(x+a)^2+(x+b)^2} + \sqrt{a^2+b^2}\right) \tag{1.4}$$

Specular Reflections

A reflector l is defined by the vector $\mathbf{r}$ defined in (1.5) containing its start point $(x_s, y_s)_l$ and its endpoint $(x_e, y_e)_l$. Reflected path delays can be expressed as (1.6)

$$\mathbf{r} = \begin{bmatrix} x_e - x_s \\ y_e - y_s \end{bmatrix} \tag{1.5}$$

$$\tau(x, y) = \frac{1}{c_0} \left(\sqrt{(x + a)^2 + (x + b)^2} \right) \tag{1.6}$$

where the constants a and b given by

$$a = \frac{2(y_e - y_s)(y_s x_e - x_s y_e)}{\|\mathbf{r}\|^2} \tag{1.7}$$

$$a = \frac{2(x_e - x_s)(y_s x_e - x_s y_e)}{\|\mathbf{r}\|^2} \tag{1.8}$$

Linear Approximation

Next the path delays from (1.6) and (1.4) are approximated by a Taylor series around a reference point x_0, y_0 [32].

$$\hat{\tau}(x, y) = \tau(x, y) + \alpha(x - x_0) + \beta(y - y_0) \tag{1.9}$$

This approximation leads to the new I/O relation (1.10).

$$\begin{aligned} \hat{y}(t, x, y) \quad \approx \quad & \sum_{l=1}^{L} \gamma_l(x_0, y_0) \\ & \exp\left(-j2\pi f_c \left(\tau_l(x_0, y_0) + \alpha_l(x - x_0) + \beta_l(y - y_0)\right)\right) \\ & s\left(t - \tau_l(x_0, y_0) - \alpha_l(x - x_0) - \beta_l(y - y_0)\right) + \omega(t) \end{aligned} \tag{1.10}$$

The complex gains are assumed to be approximately constant in a distance the order of the carrier wavelength around the reference point (1.11).

$$\gamma(x, y) \approx \gamma(x_0, y_0) \tag{1.11}$$

Algebraic manipulation lead to (1.12) and (1.13) for α and β.

$$\alpha = \frac{1}{c_0} \frac{x_0 + a}{\sqrt{(x_0 + a)^2 + (y_0 + b)^2}} \tag{1.12}$$

$$\beta = \frac{1}{c_0} \frac{y_0 + b}{\sqrt{(x_0 + a)^2 + (y_0 + b)^2}} \tag{1.13}$$

Having a look at those parameters we observe they represent the inclination of a delay over the x or y direction and have the physical unit seconds per meter $[s/m]$.

Estimation Procedure using three observations

We can estimate the parameters by evaluating at least three displaced path delays from a received CIR. This means we can reconstruct the received signals in the vicinity of the reference point x_0, y_0 on behalf of the parameters α and β estimated from at least three CIR observations.
The overall estimation procedure consists of two steps. The first step is to estimate delays from observed CIRs, while in the second step the α_l and β_l are estimated as shown in (1.14) and (1.15). Δ denotes the spacing between two grid points.

$$\hat{\alpha}_l = \frac{\hat{\tau}_l(x_0 + \Delta, y_0) - \hat{\tau}(x_0, y_0)}{\Delta} \tag{1.14}$$

$$\hat{\beta}_l = \frac{\hat{\tau}_l(x_0, y_0 + \Delta) - \hat{\tau}(x_0, y_0)}{\Delta} \tag{1.15}$$

The value of α_l or β_l can vary between $-\frac{1}{c_0}$ and $\frac{1}{c_0}$.
With α_l and β_l for each path $l = 1 \dots L$ we can reconstruct the approximate CIR for each position x and y on the grid of a region by using (1.10).
Using this novel estimation procedure the training effort would be reduced from $0.3 \cdot W^2$ to three a-priori known CIRs.

Estimation Procedure using $2W - 1$ observations

A second method to estimate α and β is presented using $2W - 1$ CIR observations. CIRs from a region can be seen as elements of a square matrix with rank W. $2W - 1$ CIRs are selected from the matrix by taking a column and a row of CIRs. The intersection of the column and the row represents the reference point x_0, y_0. We have W delay points

for each path per direction. On this points we apply the Hough transform [10] to estimate the α or β. In Chapter 4 this technique is explained more in detail. Using this novel estimation procedure for 'Spatial delay tracing' the training effort would be reduced from $0.3 \cdot W^2$ to $2W - 1$ a priori known CIRs. This method is only effective for regions with $W > 6$.

2 Parameter Estimation in an Artificial Propagation Environment

This chapter describes parameter estimation from channel impulse responses using three different algorithms. The algorithms are analyzed in terms of performance, temporal resolution and implementation effort using artificially generated channel impulse responses. Besides that the estimation of path delays and gains of artificially generated CIRs in an environment with reflectors and an environment with point-scatterers explained in Chapter 1 is investigated. The work done in this chapter can be seen as the base for the location fingerprint generation out of real measurement data in Chapter 3 and Chapter 4.

2.1 CIR parameter estimation

There exist several algorithms to estimate parameters from CIRs investigating various physical phenomena such as path delay and gains, Doppler-frequency, angle of arrival, azimuth angle, MPC decay, and so on. They all have in common that the channel impulse response is a superposition of several multipath components. This assumption is based on physical observations.

There are EM-based (Expectation Maximization) algorithms as SAGE (Space Alternating Generalized Expectation Maximization), presented in [11] which need an explicit initialization. An application of the SAGE algorithm for UWB channels referred as UWB-SAGE is presented in [13].

Algorithms which work without explicit initialization are WRELAX [19], MODE-WRELAX [28] and CLEAN-type algorithms presented in [38].

SAGE, WRELAX and MODE-WRELAX are based on the same cost function which is a least squares solution for a maximum likelihood estimate (MLE). SAGE performs an iterative solution of the MLE of the CIR parameters while WRELAX and MODE-WRELAX fragment the multidimensional optimization problem of the MLE estimator in a set of one-dimensional optimization problems. In other words they project the input sample vector on a subspace and are therefore also called subspace fitting estimation algorithms.

MODE-WRELAX is an extension to WRELAX to better resolve closely spaced overlapping signals. Algorithms using techniques based on deconvolution are CLEAN, Sensor-CLEAN and Multi-Template CLEAN presented in [7] and [38]. This approach correlates the received waveform with a unique or multiple template waveforms. The CLEAN-type algorithms count to the set of interference cancellation algorithms. It is notable WRELAX is an extension the CLEAN-type algorithms and in the original publication of the RELAX method from 1996 [24] RELAX is referred as SUPER-CLEAN. The CLEAN-type algorithms have their origins in astronomy and microwave imaging [24].

An algorithm to estimate the number of MPCs is presented in [25]. It is based on a unitary transform of the covariance matrix. Another approach uses Akaikens Information Criterion (AIC) [39]. A third approach which is based on the singular value perturbation theory is presented in [5].

2.1.1 WRELAX

WRELAX was first introduced in [19] as a conceptually simple and computationally efficient algorithm using a relaxation based minimizer of the complex nonlinear least squares criterion written in (2.10).

The cost function of the algorithm can be derived starting from a frequency domain representation (2.1) of our signal model (1.1). For simplicity the explicit location coordinates x and y is omitted here.

$$Y(k) = S(k) \sum_{l=1}^{L} \gamma_l e^{j\omega_l k} + W(k) \tag{2.1}$$

In (2.10) γ_l represents the complex gain of path l. $S(k), Y(k)$ and $W(k)$ are the discrete Fourier Transforms of the transmitted waveform, the received waveform and the additive white noise with $k = -N/2+1 \ldots N/2-1$. The discrete angular frequency ω_l is defined in (2.2) where T_s is the sampling period.

$$\omega_l = -\frac{2\pi\tau_l}{NT_s} \tag{2.2}$$

In matrix notation (2.1) can be written as in (2.3).

$$\mathbf{Y} = \mathbf{SA}\boldsymbol{\gamma} + \mathbf{W} \tag{2.3}$$

with the following definitions:

$$\mathbf{Y} = \begin{bmatrix} Y(-N/2) & Y(-N/2+1) & \ldots & Y(N/2-1) \end{bmatrix}^T \tag{2.4}$$

$$\mathbf{S} = diag\left\{ \begin{array}{cccc} S(-N/2) & S(-N/2+1) & \dots & S(N/2-1) \end{array} \right\} \tag{2.5}$$

$$\mathbf{W} = \left[\begin{array}{cccc} W(-N/2) & W(-N/2+1) & \dots & W(N/2-1) \end{array} \right]^T \tag{2.6}$$

$$\boldsymbol{\gamma} = \left[\begin{array}{cccc} \gamma_1 & \gamma_2 & \dots & \gamma_L \end{array} \right]^T \tag{2.7}$$

$$\mathbf{a}(\omega_l) = \left[\begin{array}{cccc} e^{j\omega_l(-N/2)} & e^{j\omega_l(-N/2+1)} & \dots & e^{j\omega_l(N/2-1)} \end{array} \right]^T \tag{2.8}$$

$$\mathbf{A} = \left[\begin{array}{cccc} \mathbf{a}(\omega_1) & \mathbf{a}(\omega_2) & \dots & \mathbf{a}(\omega_L) \end{array} \right] \tag{2.9}$$

According to the frequency domain signal model (2.3) a nonlinear least squares cost function can be modeled as shown in (2.10) in vector notation or in sum terms as shown in (2.11).

$$C_1(\{\gamma_l, \omega_l\}_{l=0}^L) = \left\| \mathbf{Y} - \sum_{l=1}^{L} \gamma_l \mathbf{S}\mathbf{a}(\omega_l) \right\|^2 \tag{2.10}$$

$$C_2(\{\gamma_l, \omega_l\}_{l=0}^L) = \sum_{k=-N/2}^{N/2-1} \left| Y(k) - S(k) \sum_{l=1}^{L} \gamma_l e^{j\omega_l k} \right|^2 \tag{2.11}$$

For the case of white Gaussian noise, the nonlinear least squares cost function represents the maximum likelihood estimation (MLE) method. WRELAX can be interpreted as an approximation of the MLE via a relaxation.

The WRELAX algorithm is solving this optimization problem in a relaxation based way introduced in [24]. The relaxation method referred as RELAX algorithm was introduced in [24] to solve 1-D and 2-D parameter estimation of sinusoidal waves present in autoregressive (AR) noise models.

The multidimensional nonlinear optimization problem is decomposed into multiple one-dimensional optimization problems which can be solved in a simple way.
Each of the one-dimensional optimization problems assumes all the paths except the path

we are looking for are known.

Let $\mathbf{Y}_l$ be the spectrum of path l as shown in (2.12)

$$\mathbf{Y}_l = \mathbf{Y} - \sum_{i=1, i\neq l}^{L} \hat{\gamma}_i[\mathbf{Sa}(\hat{\omega}_i)] \tag{2.12}$$

The assumption all paths except the path we are looking for are given leads to a new cost function denoted in (2.13)

$$C_3(\{\gamma_l, \omega_l\}) = \left\|\mathbf{Y}_l - \gamma_l \mathbf{Sa}(\omega_l)\right\|^2 \tag{2.13}$$

According to common estimation literature as [23] solving the minimization problem shown in (2.13) leads to (2.15) and (2.14) for the estimates $\hat{\gamma}_l$ and $\hat{\omega}_l$.

$$\hat{\omega}_l = \arg\max_{\omega_l} |\mathbf{a}^H(\omega_l)(\mathbf{S}^*\mathbf{Y}_l)|^2 \tag{2.14}$$

$$\hat{\gamma}_l = \left.\frac{\mathbf{a}^H(\omega_l)(\mathbf{S}^*\mathbf{Y}_l)}{\|\mathbf{S}\|^2}\right|_{\omega_l=\hat{\omega}_l} \tag{2.15}$$

WRELAX determines the estimates by the sequence shown in Figure 2.1. We start with $\mathbf{Y}_1$ for the first value for $\mathbf{Y}$.

1.	L = 1, compute $\hat{\gamma}_1$ and $\hat{\omega}_1$ from (2.15) and (2.14).
2.	L = 2, compute $\mathbf{Y}_2$ by using $\hat{\gamma}_1$ and $\hat{\omega}_1$ with (2.12)
3.	L = 2, compute $\hat{\gamma}_2$ and $\hat{\omega}_2$ using $\mathbf{Y}_2$ with (2.15) and (2.14)
4.	L = 2, compute $\mathbf{Y}_1$ by using $\hat{\gamma}_2$ and $\hat{\omega}_2$ with (2.12)
5.	L = 2, compute $\hat{\gamma}_1$ and $\hat{\omega}_1$ using $\mathbf{Y}_1$ with (2.15) and (2.14)

Figure 2.1: WRELAX estimation procedure

The five steps of Figure 2.1 are repeated until practical convergence is reached. Then a new path is added to the estimation sequence in the same way. All obtained results are used for the estimates of the new path. Next all the other estimates are recalculated with the new estimates. This procedure is repeated until the desired number of paths is reached.

The relative change in the cost function (2.10) determines the practical convergence. How fast the algorithm converges depends on the delay between the paths desired to estimate.

The reiterations after each added paths are an important feature of the WRELAX algorithm. Each result obtained after a path is a good initialization for the next path. If we set the number of reiterations to zero the WRELAX algorithm becomes the CLEAN algorithm presented in [7].

Another interesting feature of the WRELAX algorithm is that it needs no explicit parameter initialization.

Due to the operation of WRELAX in the frequency domain it has no influence whether Complex baseband or passband signals are used.

WRELAX Implementation

The pseudo code of the WRELAX implementation is shown in 2.1. The minimal relative change in the cost function is set to 10^{-4}, which delivered good results. The numerical computing environment MATLAB®is used for implementation.

Listing 2.1: WRELAX pseudocode

```
Y_l = Y
γ̂_{1...L} = 0
τ̂_{1...L} = 0

for l = 1:L
  % initial estimate
  if l > 1
    Y_l = Y − Σ_{i=1,i≠l}^{L} γ̂_i [Sa(ω̂_i)]
  end

  ω̂_l = arg max_{ω_l} |a^H(ω_l)(SY_l)|^2
  γ̂_l = a^H(ω_l)(SY_l) / ||S||^2 |_{ω_l=ω̂_l}

  % add paths iteratively
  if kLp > 1
    maxloop = 4;
    while loopcount < maxloop && |c−c_old| / c_old > 10^{-4}
      c_old = c
```

```
        % update all old estimates
        for k = 1:l
            Y_k = Y − Σ_{i=1,i≠k}^{l} γ̂_i[Sa(ω̂_i)]
            ω̂_k = arg max_{ω_k} |a^H(ω_k)(SY_k)|^2
            γ̂_l = a^H(ω_l)(SY_l) / ||S||^2 |_{ω_l=ω̂_l}
        end
    end

    c = ||Y − Σ_{i=1}^{L} γ̂_i[Sa(ω̂_i)]||^2
end

τ̂ = −ωT_CIR / 2π
```

2.1.2 MODE-WRELAX

The MODE-WRELAX algorithm is a combination of the Method of Direction Estimation (MODE) algorithm first presented in [35] and the WRELAX algorithm described above. The main goal of the algorithm is it to gain a better accuracy than MODE and a higher time resolution then WRELAX combining both algorithms sequentially [28].
MODE tries to minimize the same cost function (2.10) as WRELAX is derived from. First the parameter space is replaced, then the resulting cost function will be approximated by a quadratic function.

We derive the MODE algorithm starting from the WRELAX cost function (2.10) in vector notation (2.16)

$$C_3(\{\gamma_l, \omega_l\}_{l=0}^{L}) = \left\| \mathbf{Y} - \mathbf{SA}\boldsymbol{\gamma} \right\|^2 \tag{2.16}$$

This can be rewritten in a form of a projection of Y on a subspace.

$$C_4(\{\gamma_l, \omega_l\}_{l=0}^{L}) = \mathbf{Y^H P_A Y} \tag{2.17}$$

where

$$\mathbf{P_A} = \mathbf{I} - \mathbf{SA}(\mathbf{S^H A^H SA})^{-1}\mathbf{S^H A^H} \tag{2.18}$$

This cost function is reparameterized in terms of ω_l by a set of parameters b_l.

$$b_0 z^L + b_1 z^{L-1} + ... + b_L = b_0 \prod_{l=1}^{L} (z - e^{j\omega_l}) \tag{2.19}$$

$$b_0 \neq 0 \tag{2.20}$$

The polynomial (2.19) has its zeros on the unit circle and its coefficients b_l satisfy the symmetry constraint (2.21) [35].

$$b_l = b^*_{L-l}, \qquad l = 0, 1, \ldots, L \tag{2.21}$$

Let the matrix $\mathbf{B}$ be our new data matrix

$$\mathbf{B} = \begin{bmatrix} b_0 & & 0 \\ \vdots & \ddots & \\ b_L & & b_0 \\ & \ddots & \vdots \\ 0 & & b_L \end{bmatrix} \tag{2.22}$$

Now the relationship

$$\mathbf{B^H A} = \mathbf{0} \tag{2.23}$$

holds and we can write the cost function with the new parameter space where $\mathbf{P_A}$ can be rewritten as

$$\mathbf{P_A} = \mathbf{S^{-H}B}(\mathbf{S^{-1}B^HS^{-H}B})^{-1}\mathbf{B^{-1}B^H} \tag{2.24}$$

We write the cost function over the new parameter space

$$C_5(\{\gamma_l, \omega_l\}_{l=0}^{L}) = \mathbf{Y^H S^{-H}B}(\mathbf{S^{-1}B^HS^{-H}B})^{-1}\mathbf{B^{-1}B^HY} \tag{2.25}$$

The term $(\mathbf{S^{-1}B^HS^{-H}B})^{-1}$ is seen as a consistent estimate which is not affecting the asymptotically statistical efficiency of the minimizer. It is replaced by $(\mathbf{S^{-1}B_0^HS^{-H}B_0})^{-1}$ depending only on the initial estimate $\mathbf{B_0}$. Therefore the cost function can be rewritten as

$$C_6(\{\gamma_l, \omega_l\}_{l=0}^{L}) = \mathbf{Y^H S^{-H}B}(\mathbf{S^{-1}B_0^HS^{-H}B_0})^{-1}\mathbf{B^{-1}B^HY} \tag{2.26}$$

This reduces the cost function C_5 to a quadratic function C_6 which is computationally easier to minimize. In the original paper [35] where MODE is introduced the above term

is labeled as a weighting matrix. The search over the new parameter space is computationally more efficient [28].

The minimizer of the cost function can be written as

$$\mathbf{b} = \arg\min_{\mathbf{b}}[\mathbf{Y^H S^{-H} B}(\hat{\mathbf{B}}_\mathbf{0}^\mathbf{H}\mathbf{S^{-1}S^{-H}}\hat{\mathbf{B}}_\mathbf{0})^{-1}\mathbf{B^H S^{-1}Y}] \tag{2.27}$$

The initial estimate is obtained

$$\mathbf{b_0} = \arg\min_{\mathbf{b}}[\mathbf{Y^H S^{-H} B B^H S^{-1}Y}] \tag{2.28}$$

The trivial solution $\mathbf{b} = \mathbf{0}$ is avoided by using the constraint

$$\|\mathbf{b}\| = 1 \tag{2.29}$$

The MODE algorithm is not an iterative algorithm in common sense, it has no convergence criterion.

Once the parameter vector $\mathbf{b}$ is obtained the estimates $\hat{\omega}_l$ are the phases of the roots of the polynomial (2.19).

The estimated path-gains γ_l can be computed according to (2.30)

$$\mathbf{Y} \approx \mathbf{S}\hat{\mathbf{A}}\boldsymbol{\gamma} \tag{2.30}$$

This can be done by solving the linear least squares problem, e.g. using QR decomposition [27].

MODE-WRELAX uses the estimates $\{\hat{\gamma}_l, \hat{\omega}_l\}_{l=1}^{L}$ obtained from MODE as the initial estimates for the WRELAX algorithm. Calculate $\mathbf{Y}_1$ from $\{\hat{\gamma}_l, \hat{\omega}_l\}_{l=2}^{L}$ obtained from MODE than continue the WRELAX estimation sequence as shown in Figure 2.1.

MODE-WRELAX Implementation

The MODE-WRELAX implementation is shown in listing 2.2. The MATLAB®function fmincon was used to solve the minimization problem. The author of [28] considers iterating a couple of times over the minimizer. In our implementation we used 4 iterations.

Listing 2.2: MODE-WRELAX pseudocode

```
% MODE
iterations = 4
```

```
% initialization
β̂_0 = arg max_β β^H Re( Γ^H Ṽ^H Ṽ Γ ) β

for i = i:iterations
    β = β_0
    β = arg min_β β^H Re[ Γ^H Ṽ^H ( B̂_0^H S^-1 S^-H B̂_0 )^-1 Ṽ Γ ] β
end

ω̂ = angle( roots(Γβ) )

for l = 1:L
        a(ω̂(l)) = exp(-iω̂(l))
        Â(:,l) = a(ω̂(l))
end

γ̂ = Y\SÂ

% WRELAX (pseudocode shown in WRELAX listing)
[ω̂, γ̂] = wrelax(Y, ω̂, γ̂)
τ̂ = -ωT_CIR / 2π
```

2.1.3 SAGE

The SAGE algorithm (space-alternating generalized expectation maximization) is an extension to the expectation maximization method [9], which provides an iterative method to solve the ML estimation problem. It was applied to mobile radio environments in [11] to jointly estimate relative delays, incidence azimuth, Doppler frequency and complex amplitudes. In [13], the algorithm is applied to the UWB indoor channel and referred to as UWB-SAGE. A statistical UWB channel model based on SAGE estimation is presented in [31].

The EM algorithm consists of an E (Estimation) and an M (Maximization) step. The E-step represents the signal decomposition, while in the M-step the ML estimation of a single impinging wave is performed.

The received signal $y(t)$ represents the incomplete but observable data which is com-

posed by a set of unobservable complete data $x_l(t)$ as shown in (2.32).

$$y(t) = \sum_{l=1}^{L} x_l(t) \tag{2.31}$$

Each part of the complete data can be seen as a signal corrupted by a part of additive noise

$$x_l(t) = s(t;\theta_l) + w_l(t) \tag{2.32}$$

where our parameters (delays and gains) to be estimated for the lth path are given by

$$\theta_l = [\tau_l, \gamma_l], \tag{2.33}$$

While all estimates for the received CIR are given by

$$\theta = \left[\begin{array}{ccc} \theta_l & \dots & \theta_L \end{array} \right]. \tag{2.34}$$

The M-step of the algorithm computes and maximizes the cost function (2.35) where $p(t)$ denotes the transmitted pulse shape, while in the E-step the complete data is updated with the estimates of the E-step (2.36).

$$z(\tau_l, \alpha_l) = |p(t) * x_l(t)| \tag{2.35}$$

$$x_l(t;\hat{\theta}') = s_l(t;\hat{\theta}'_l) + y(t) - \sum_{l=1}^{L} s_l(t;\hat{\theta}'_{l'}) \tag{2.36}$$

SAGE Implementation

The implementation showed in 2.3 was provided by [14] and reduced for only estimating delays and complex gains. The used SAGE implementation has a variable to set a number of forbidden samples before and after a detected path to avoid multiple detection on large bandwidths.

Listing 2.3: SAGE pseudocode

```
% Initialization
x_l(t) = y(t)
```

```
for l=1:L
   z(t;τ_init) = xcorr(p*(t),x_l(t))
   τ_l = arg max|z(t;τ_init)|
   α_l = (MP)^{-1} · p(t) · x_l(t)
   s_l(t) = α_l p(t − τ_l)

   x_l(t) = y(t) − Σ_{l=1}^{L} s_l(t)
end

% SAGE
for μ = 1:cycles
   for l=1:L
      % M–step
      z(t;τ_init) = xcorr(p*(t),x_l(t))
      τ_l = arg max|z(t;τ_init)|
      α_l = (T_p P_u)^{-1} · p(t) · x_l(t)
      s_l(t) = α_l p(t − τ_l)

      % E–step
      x_l(t) = s_{μ mod L+1}(t) + y(t) − Σ_{l=1}^{L} s_l(t)
   end
end
```

2.2 Performance Evaluation

Artificial CIRs with Gaussian and sinc-shaped pulses are used to test the performance of the algorithms. The discrete time CIRs $\mathbf{y} = [\ y[1] \quad \dots \quad y[N]\ ]^T$ are sampled versions of $y(t)$ written in (2.37). The performance of the delay estimation is primarily important for our tasks. Therefore the performance of the gains estimation is not investigated. The number of forbidden samples for the SAGE algorithm is set to 2. We define a Gaussian pulse as written in (2.38).

$$y(t) = \sum_{l=1}^{4} \gamma_l g(t - \tau_l) \tag{2.37}$$

$$g(t) = e^{-\frac{(t-\tau)^2}{\kappa^2}}. \tag{2.38}$$

The signal bandwidth defines the parameter κ of the Gauss-pulse according to (2.39) [36].

$$\kappa = \frac{1}{\pi BW \sqrt{\log(e)}}. \tag{2.39}$$

The sinc pulse is defined as $g(t) = \mathrm{sinc}(BW(t-\tau))$. The bandwidth is set to 2 GHz, the sampling frequency to 4 GHz which results in 100 samples for 25 ns. Figure 2.2 and 2.3 show the artificial CIRs used to test the WRELAX algorithm. The DFT magnitude of both CIRs is shown in Figure 2.4. Besides the pulse shape various values for SNR and the bandwidth are investigated.

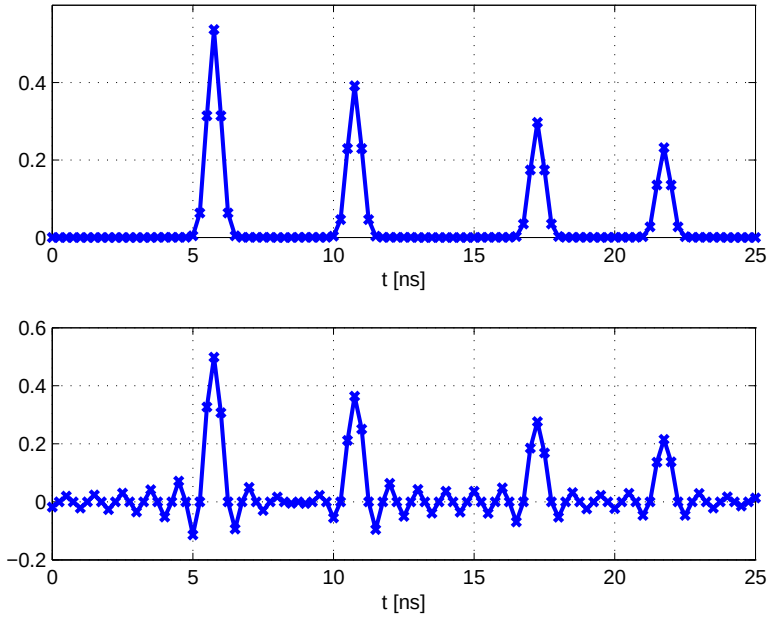

Figure 2.2: Distant Gaussian and sinc pulses

To perform the SNR simulation we corrupt our CIRs with AWGN (2.40) with a variance σ^2 defined in (2.40). To obtain statistically reliable results we average over 500 noise realizations.

$$\sigma = \sqrt{\frac{E_b}{SNR}} \tag{2.40}$$

$$w(t) \sim \mathcal{N}(0, \sigma^2) \tag{2.41}$$

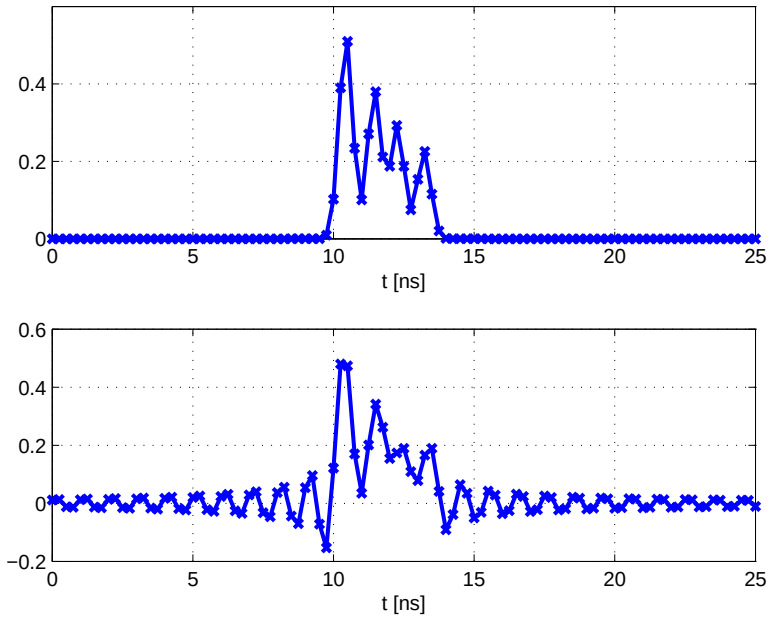

Figure 2.3: Near-by Gaussian and sinc pulses

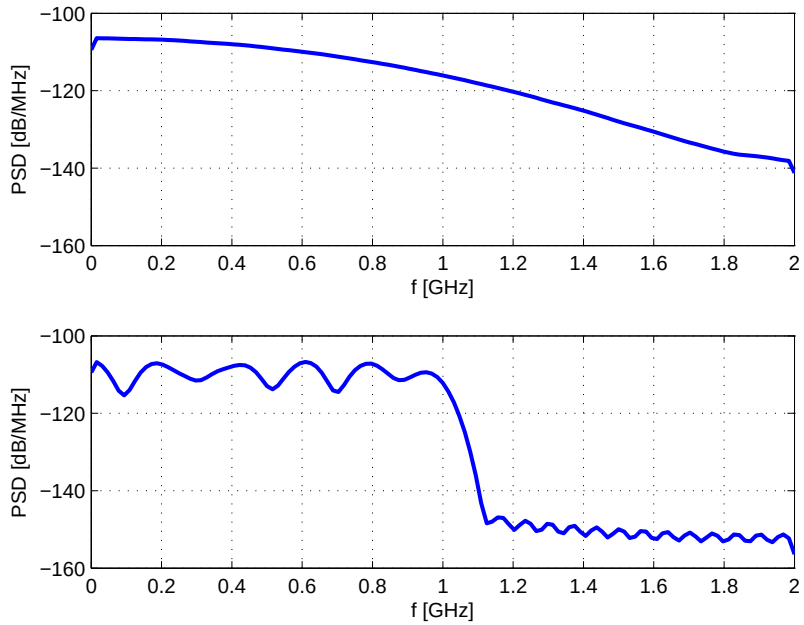

Figure 2.4: Spectra of Gaussian and sinc pulse

2.3 Results

The MODE algorithm achieves good results for high SNR values, but totally fails for lower SNR values where WRELAX and SAGE still perform well. Since in the MODE-WRELAX algorithm MODE initializes WRELAX this results in bad performance. There-

fore, the MODE-WRELAX algorithm is not taken into account for the SNR study. The root mean squared error (RMSE) is defined as

$$RMSE = \sqrt{E\left\{(\tau_l - \hat{\tau}_l)^2\right\}} \tag{2.42}$$

For the distant pulses from Figure 2.2 WRELAX and SAGE achieve the same performance results if time delay equals time sample as shown in Figure 2.5. If this is not the case WRELAX outperforms SAGE because its search resolution is not restricted to discrete time samples. This effect is shown in Figure 2.6. For the close pulses from Figure 2.3 where the peak of the pulses lies somewhere between two time samples WRELAX performs better than SAGE. SAGE reaches a bias because it takes the next sample. There is no significant difference between the performance of the Gauss pulse and the sinc pulse.

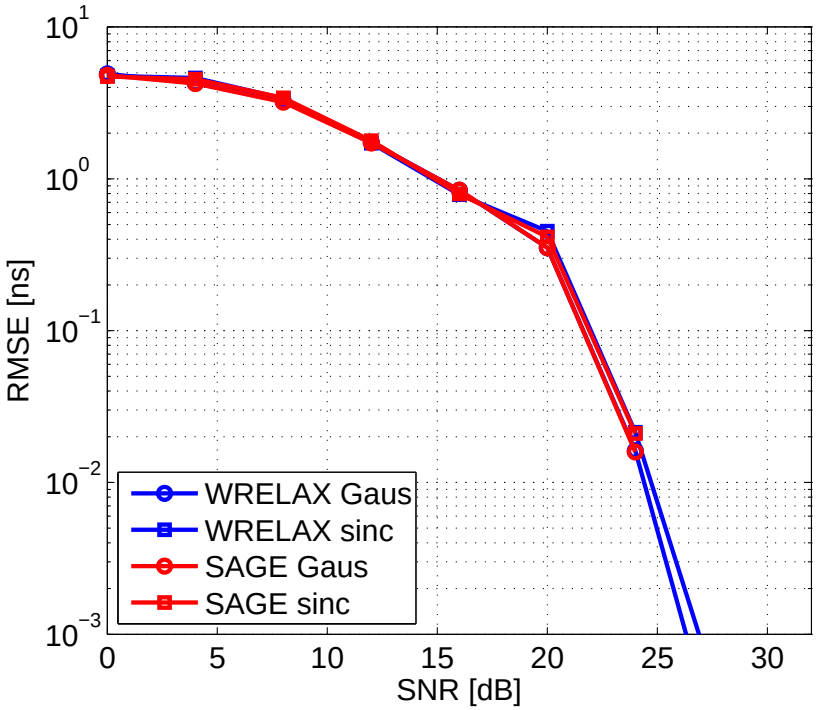

Figure 2.5: WRELAX vs. SAGE performance for distant pulses

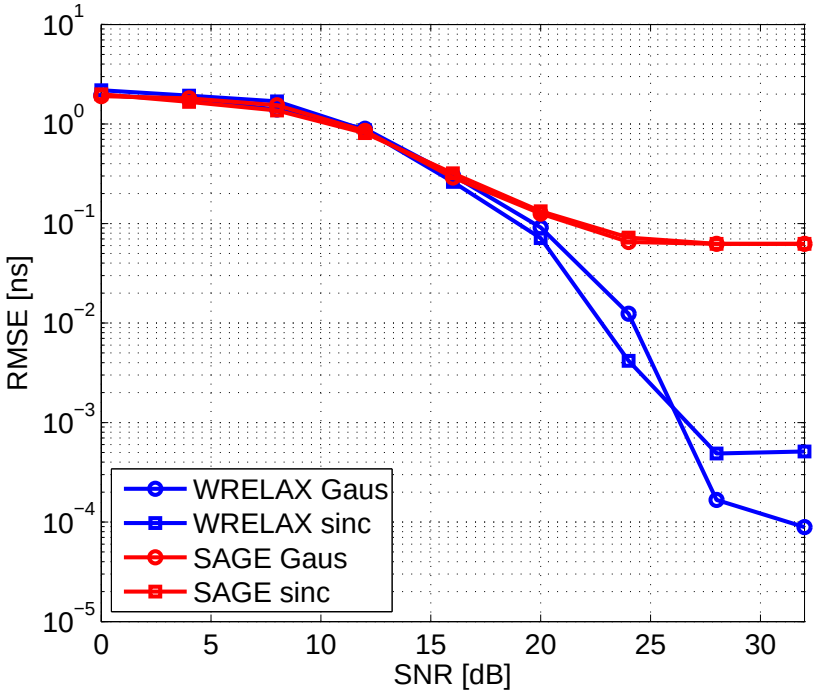

Figure 2.6: WRELAX vs. SAGE performance for close pulses

2.3.1 Performance Evaluation of α and β estimation

The estimation was performed in two artificial environments, one representing a reflection and one a scattering environment as displayed in Figures 2.7 and 2.8.

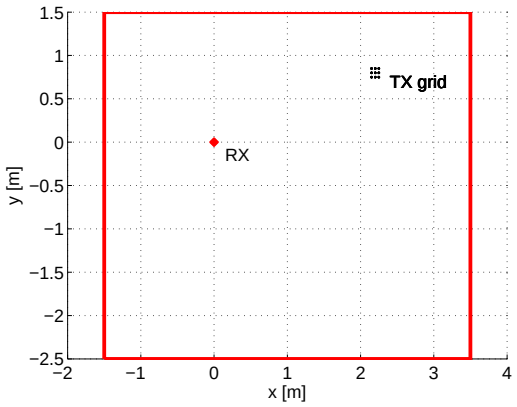

Figure 2.7: Simulation environment for the reflection scenario with specular reflecting walls

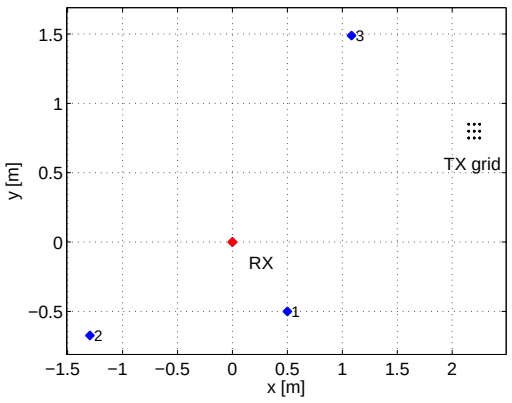

Figure 2.8: Simulation environment for the diffraction scenario with 3 point scatterers

Exact delays are calculated according to the ray tracing formulas presented in Chapter 1. Our goal is to perform an SNR study of the estimated delays vs. the calculated delays and the performance of the estimated $\hat{\alpha}$ and $\hat{\beta}$ vs. the exact $\hat{\alpha}$ and $\hat{\beta}$. The mean over all delays can be used for comparison or simply the delay for a single reflection or scattering event. The reflectors act as specular reflectors. The scattering points have a randomly chosen sign of the gain value. The gain value itself is computed using the average free space path loss formula over the bandwidth (2.43). This formula is obtained by integrating over Friis equation for path loss [12] and dividing trough the bandwidth. The according gains γ are calculated as shown in (2.44) on behalf on the path loss. d_l is a constant value representing the attenuation coefficient with random sign.

$$FP = \sqrt{\frac{\left(\frac{0.5*3e8}{4\pi}\right)^2}{f_c^2 - \frac{BW^2}{4}}} \tag{2.43}$$

$$\gamma_l = d_l \frac{FP}{\tau_l} \tag{2.44}$$

The generated CIRs from the exact delays from the ray tracing equations were corrupted by additive Gaussian noise and fed to the WRELAX algorithm.

The performance of the α and β estimation depends directly on the performance of the path-delay estimation as we can see in Figure 2.9. Table 2.1 and Table 2.2 show the

accuracy of the estimation for the 30 dB SNR case. The columns indicate the reflected paths from the four walls in the reflection scenario and the scatterd paths from the scattering points. The direct path (LOS) is shown also. For each path the exact, the estimated and the difference between the exact and the estimated value is displayed for delays, α and β. The exact delay values are calculated from the environment via ray tracing, while the estimated delay values are the outcomes of the WRELAX algorithm. By nature the parameters α and β have the unit s/m. To make things more visible they are multiplied with the c_0. This implies a delay change of 0.033 ns over a distance of 1 cm for a α or β value of one.

		LOS	1	2	3	4
$\tau_{x_0,y_0,l}$ [ns]	exact	7.5902	10.3736	16.3588	17.3478	20.4627
	est.	7.5893	10.3687	16.3546	17.3464	20.4615
	diff.	0.0009	0.0048	0.0042	0.0014	0.0012
α_l	exact	-0.9430	-0.687	0.988	-0.989	-0.347
	est.	-0.930	-0.660	0.974	-0.854	-0.276
	diff.	-0.013	-0.027	0.014	-0.135	-0.071
β_l	exact	-0.320	0.727	-0.148	-0.139	-0.936
	est.	-0.321	0.767	-0.138	-0.099	-0.924
	diff.	0.002	-0.041	-0.010	-0.040	-0.012

Table 2.1: α and β results for reflection scenario with Gaussian pulses and an SNR of 30 dB

		LOS	1	2	3
$\tau_{x_0,y_0,l}$ [ns]	exact	7.5902	9.2571	12.2284	15.6196
	est.	7.5915	9.2593	12.2245	15.6239
	diff.	-0.0013	-0.0022	0.0038	-0.0043
α_l	exact	-0.943	-0.793	-1.000	-0.981
	est.	-0.942	-0.820	-0.963	-1.015
	diff.	-0.001	0.027	-0.037	0.033
β_l	exact	-0.320	-0.596	-0.005	0.198
	est.	-0.333	-0.604	0.004	0.172
	diff.	0.013	0.008	-0.009	0.026

Table 2.2: α and β results for scattering scenario with Gaussian pulses and an SNR of 30 dB

The Tables for the sinc pulse show similar performance values. They can be found in Appendix A.

The RMSE for this evaluation is defined in (2.45) and (2.46). Where α and β is calculated from the exact delays and $\hat{\alpha}$ and $\hat{\beta}$ from the estimated delays.

$$RMSE = \sqrt{E\left\{(\alpha_l - \hat{\alpha}_l)^2\right\}} \tag{2.45}$$

$$RMSE = \sqrt{E\left\{(\beta_l - \hat{\beta}_l)^2\right\}} \tag{2.46}$$

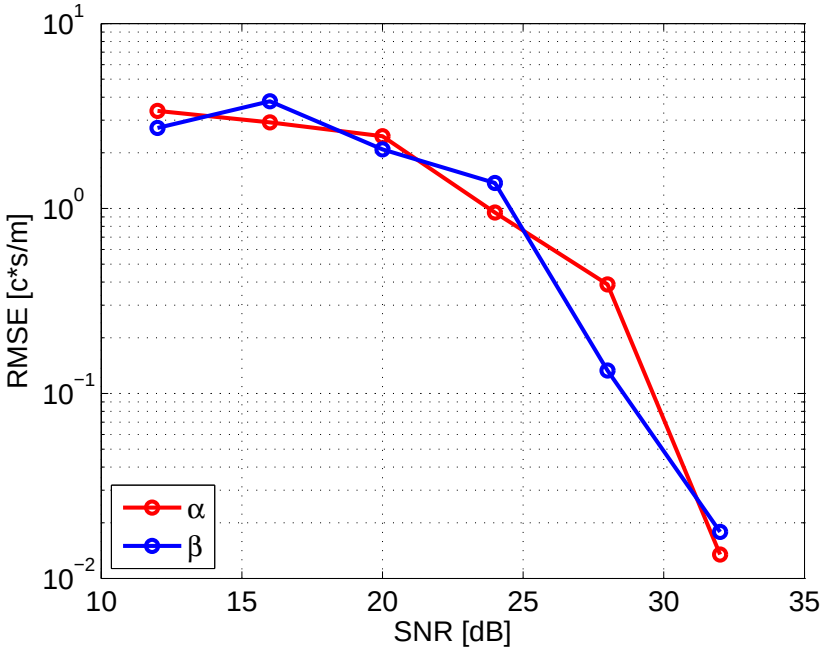

Figure 2.9: RMSE of α and β values over SNR with a bandwidth of 2 GHz, $\Delta = 0.05$ m for the Gaussian pulse in the scattering scenario

The bandwidth of the transmitted pulses determines the width of the pulses. The narrower the pulses are, the less spacing can be between the received paths. In our investigated environments the shortest delay between two paths is 2 ns in the scattering environment. Therefore the bandwidth generating pulses which are not narrow enough to resolve those paths lead to a bad performance as shown in Figure 2.10. The RMSE in this Figure is defined in (2.42). On lower bandwidth the Gaussian pulse shows a better performance. A possible explanation for this is that the side lobes of the sinc pulse have a negative effect on the performance.

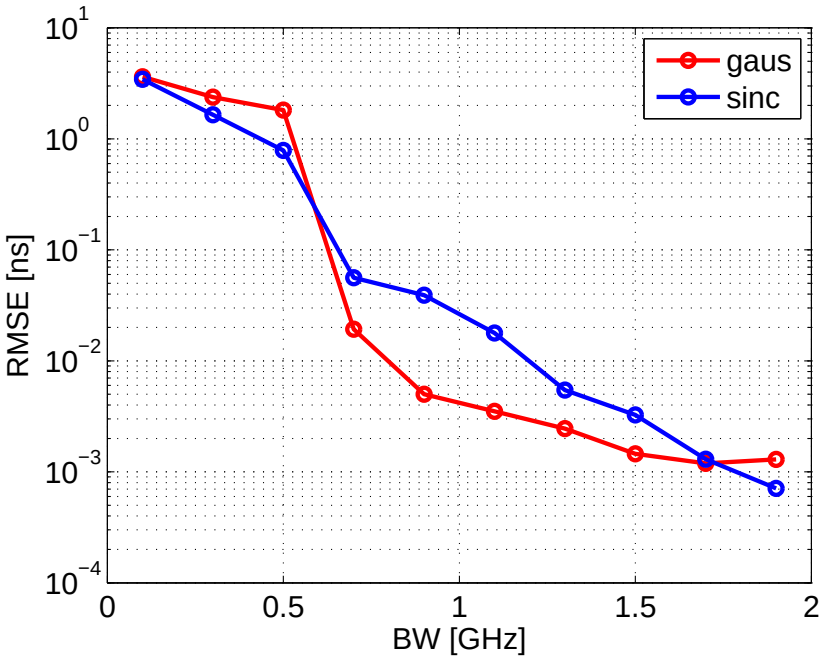

Figure 2.10: RMSE over all paths for signal bandwidths from 0.1 to 1.9 GHz with a Gaussian pulse for the scattering environment, an SNR of 30 dB and $\Delta = 0.05$ m

2.4 Conclusion

With a sufficiently high SNR level the estimation of the α and β generates a low error. The quality of the estimation depends directly on the quality of the time delay estimation. For delay estimation we choose WRELAX to be the most applicable algorithm. Its resolution is not limited to time samples and it performs well on closely spaced paths.
As expected no difference between the reflection and the scattering scenario is observable because in both cases the exact delays are calculated according to deterministic ray tracing formulas.
WRELAX is robust against different path shapes as the authors mention [19]. Nevertheless for bandwidths from 0.5 GHz to 1.5 GHz the sinc pulse shows a lower accuracy than the Gaussian pulse.

3 Fingerprint Generation from AEC Measurements

This chapter investigates the procedure to gather location fingerprints from spatio-temporal CIR measurements in an anechoic chamber with an artificial reflection environment as shown in Figure 3.1. This procedure includes the measurement scenario, post processing of the measurement data and estimation of the necessary parameters.
CIR measurements are acquired on a square grid from which the delays are estimated using the WRELAX algorithm. Time delays from the reflectors are estimated from the CIRs. The delays are used further to estimate the parameters α and β. On behalf of the parameters α and β we generate artificial CIRs for each point on the grid. Fingerprints from both measured and artificial CIRs are generated and compared.

Figure 3.1: Reflection Environment for Scenario 3 with two reflectors and positioning device

3.1 AEC Channel Measurement Campaign

The goal of the measurement campaign was to capture CIRs generated by a controlled channel with two reflectors in the anechoic chamber at ETH Zürich in building ETF, Floor Z.
We perform a cross-correlation between the received signal and the known transmit signal in order to obtain the impulse responses. The cross correlation can be written as the circular convolution (3.1) where $x[n]$ is the received signal and $s[n]$ the known transmit signal. The transmit signal $s[n]$ is a PN (pseudo noise) sequence with length $2^{15} - 1$.

$$y[n] = x[n] \circledast s[-n] \tag{3.1}$$

Since $s[n]$ is real valued we can write the discrete spectra (3.2)

$$Y[k] = S^*[k]X[k] \tag{3.2}$$

and get the impulse response by taking the inverse discrete Fourier transform (3.3).

$$y[n] = F^{-1}\{S^*[k]X[k]\} \tag{3.3}$$

3.1.1 Measurement Setup

Figure 3.2 shows the basic setup of the measurement campaign. Information about the components can be found in Table 3.1 and 3.2.
Different transmitter locations and reflector constellations were used. The geometry of the reflectors and the position of the receiver and the transmitter were measured by using a laser measurement device and a measuring tape.

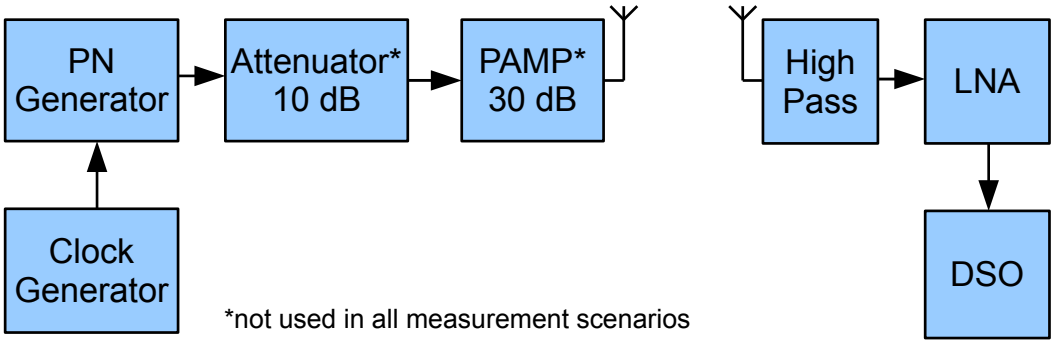

Figure 3.2: Measurement Setup

A precise computer aided positioning device was used to place the transmit antenna on positions at the 28 times 28 cm grid with a spacing of 1 cm between each grid point. Every stored CIR is the average over 20 CIR-measurements recorded by the oscilloscope. Averaging over more than 20 measurements resulted in no significant increase of quality. To be able to use the antenna orientation with the maximum radiation strength several orientations were investigated. The orientation with the highest gain was chosen for the campaign.

Parameter	Value
Sampling Rate	50 GS/s
Horizontal resolution	1 μs/div
Vertical resolution	10 mV/div (200 mV/div with PAMP)
Antenna height	1.95 m
PN Clock rate	8 GHz
PN Order	15
PN Sequence duration	$(2^N - 1)\frac{1}{8GHz} \approx 4.1\mu s$
PAMP Gain	30 dB
PAMP Bandwith	2 - 8GHz
PAMP Power	30 dBm
Highpass	Loss: under 1dB over 910 MHz

Table 3.1: Measurement Parameters

Component	Denotation
PN Generator	Centellax TG1P1A
UWB antennas	Skycross SM3TO10MA
Waveform Generator	Tektronix AWG7102
Oscilloscope	Tektronix DPO 72004
PAMP	Mini Circuits ZVE-8G
Highpass Filter	Mini Circuits SHP900

Table 3.2: Measurement Components

3.1.2 Measurement Scenario

The measurement campaign was subdivided into following scenarios.

- Scenario 1: without PAMP, without positioning device, without reflectors
- Scenario 2: with PAMP, without positioning device, without reflectors

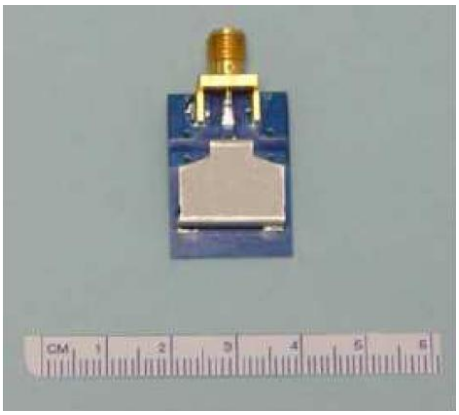

Figure 3.3: Skycross UWB Antenna

- Scenario 3: with positioning device
    1. Averaging, without reflectors, with PAMP
    2. Averaging, without reflectors, without PAMP
    3. Configuration from Figure 3.4, with PAMP
    4. Configuration from Figure 3.4 (Env. 1), without PAMP
    5. Configuration from Figure 3.5 (Env. 2), without PAMP

Scenario one and two were used to get to know the behavior of the measurement system and to eliminate unwanted peaks in the CIR from reflections in cables and connection parts by testing different constellations of amplifiers and filters and mounting RF shielding material around the antennas. The influence of the light in the chamber on our measurements was also investigated. There was no measurable difference between the light off or on.

In scenario three the main measurements were performed. For each of the five points from the third scenario 784 CIR signatures were stored. In order to get reliable results from the path-delay and gain estimation algorithms the acquisition of a reference pulse without any reflections was necessary. We performed scenario one and two without reflectors over all positions. In the post processing we obtain the reference pulse $y_B[n]$ by taking the mean over the CIRs from all TX positions without reflectors. In this way unwanted reflections are eliminated.
In the last two scenarios, measurements with and without power amplifier (PAMP) were performed. The Scenarios with PAMP have a transmit power of -14.8 dBm/MHz at the antenna and show an average SNR of 72.5 dB. This parameters do not follow the FCC regulations for UWB. Without PAMP the average SNR is 56.6 dB and the transmit power at the antenna is -34.8 dBm/MHz which is close to the FCC regulations which allow -41.3 dBm/MHz. The estimated spectra are shown in Figure 3.6.

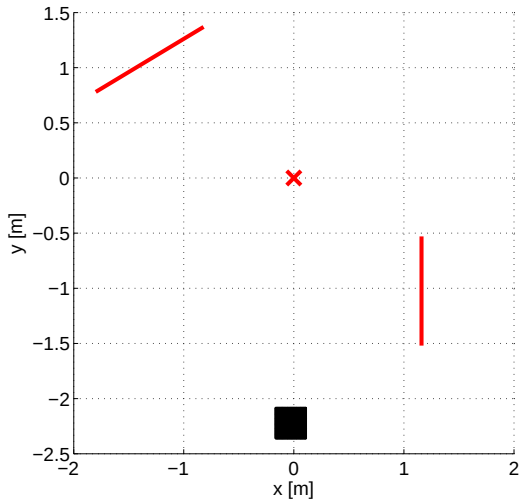

Figure 3.4: Reflector configuration for Env. 1, the red cross denotes the RX antenna, the black square the TX grid

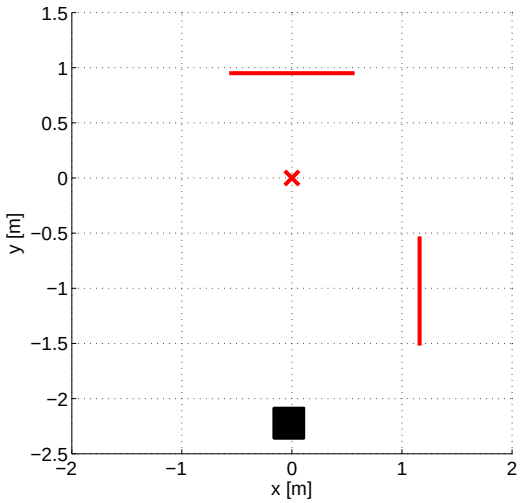

Figure 3.5: Reflector configuration for Env. 2, the red cross denotes the RX antenna, the black square the TX grid

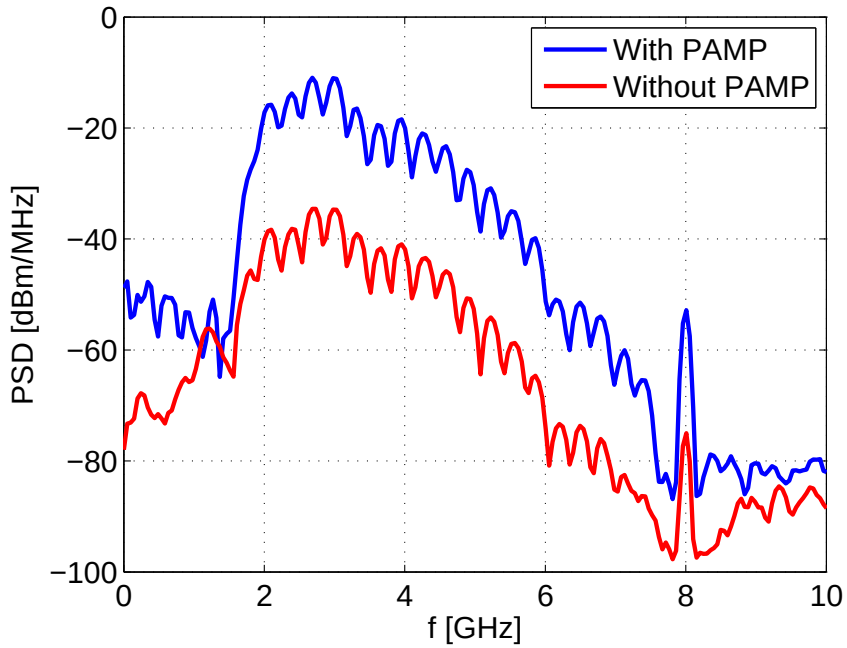

Figure 3.6: Pwelch Power spectral density for the measured CIRs with an without pre-amplifier

3.2 Postprocessing

The processing of the raw signatures leads to the desired parameters used to describe a location fingerprint. On one side fingerprints based on measured CIR signatures are produced and on the other side fingerprints based on artificially generated CIR signatures are produced. Therefore two ways can be distinguished.

The first way shown in Figure 3.7 takes the raw CIR signatures, aligns, cuts, filters them and estimates the mean vector μ and the covariance matrix $\mathbf{\Sigma}$. For the estimation 0.3×28^2 CIRs are used.

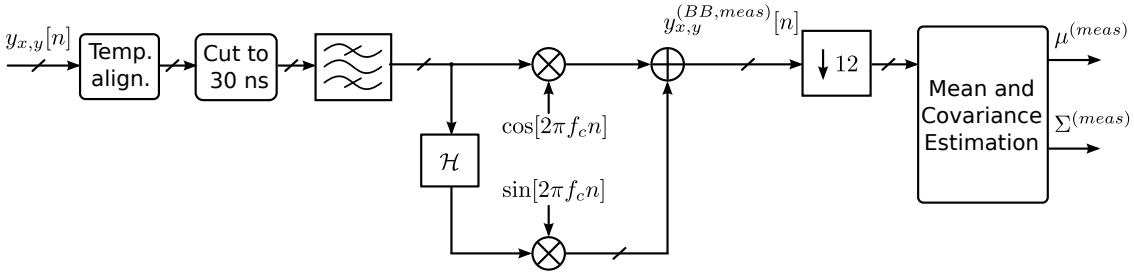

Figure 3.7: Postprocessing and parameter generation signal flow of measured CIRs

The second way shown in Figure 3.8 takes only three of the measured signatures, post processes them in the same fashion as in the first way, estimates values α_l and β_l for each reflection l of each of the threes signatures. The rest of the signatures is generated artificially on behalf of the estimated values. The estimation of the mean vector μ and the covariance matrix $\mathbf{\Sigma}$ is done as in the first way by using the artificially generated CIRs.

The used measurement setup delivered no absolute timing information for the measured CIRs. Therefore a temporal alignment step was necessary. Two methods of temporal alignment were implemented. One method simply aligns the strongest path of the CIR to a reference sample. This simple temporal alignment procedure works for the AEC signatures, because it is guaranteed the first path is the strongest path. This type of temporal alignment has the advantage to be very simple. The main disadvantage is that the α and β estimates of the LOS component are set to zero, even if it is not true. This causes estimates for path delays caused by reflectors placed orthogonal to the line drawn from the transmitter to the receiver antenna are either twice as high as they would be by using a time reference or zero. Hence with this method the values for α and β lie within -2 to 2.

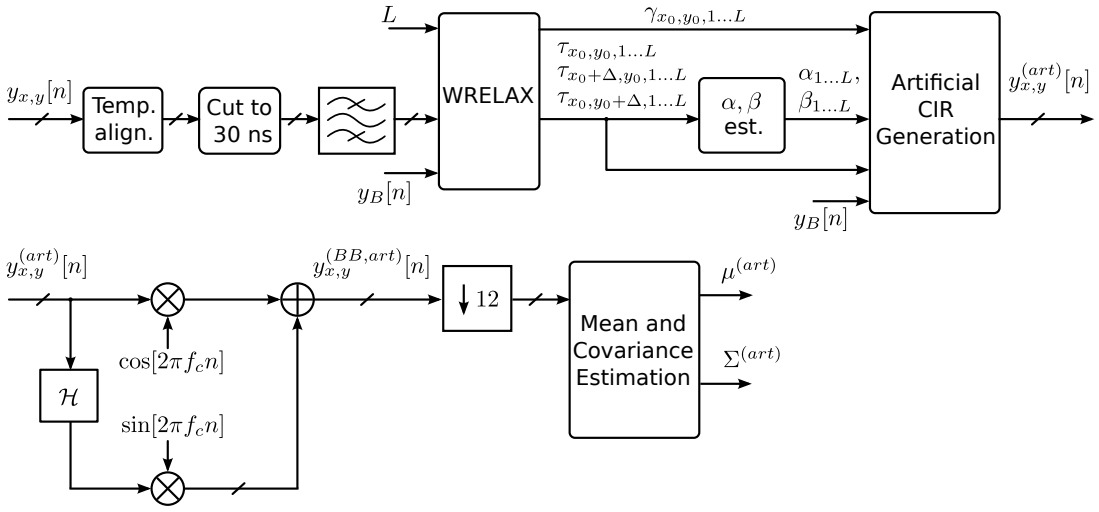

Figure 3.8: Postprocessing and parameter generation signal flow of artificial CIRs

The second method is an extended temporal alignment procedure which includes the exact delays on the TX grid. This method is aware of the spatial movement of the transmitter. The geometry of the TX grid and the position of the transmitter relative to the receiver antenna must be known. This method effectuates the mean of the CIRs is near zero.

After the alignment samples after 30 ns were dropped because a reflection with such a long delay would not be realistic for environments in this dimension. This leads to 5000 sampling points per CIR. Next the signal was filtered with a bandpass-filter to eliminate interferences from outside of our bandwidth. A Parks-McClellan optimal equiripple FIR order estimator was used to calculate the coefficients. The stop band cut-off frequency at the lower edge of our frequency band was set to 1.6 GHz, the passband cut-off frequency to 2 GHz. Analog at the upper edge of our band the stop band cut-off frequency was set to 6.4 GHz and the passband cut-off frequency to 6 GHz. The stop band attenuation of the filter is 40 dB the resulting filter order 179. The estimated spectrum of the unfiltered signals are shown in Figure 3.6 while the spectrum of the filtered signal (without PAMP) is shown in Figure 3.11.

In the second way next the filtered CIRs are delivered to the WRELAX algorithm (see Chapter 2) which returns the delays τ_l of L paths from the impulse responses. For the AEC measurement the number of paths L is known because no paths except the paths

from the reflectors apprear.
WRELAX is an algorithm based on a known reference pulse (also referred as base pulse in this work). Therefore in addition to the measured CIRs also the base pulse is required. The base pulse is the LOS path in the AEC since no other reflections occur. The reference pulse $y_B[n]$ is obtained by averaging over all 28^2 captured CIRs from the third scenario (point 1 and 2, with and without PAMP, without reflectors).
For the estimation of the parameters α and β the delays from at least at least three CIRs have to be estimated as known from Chapter 2.
According to the signal model (1.10) the artificial CIRs $y_{x,y}^{(art)}[n]$ for each grid point can be generated by calculating the necessary delays on behalf of $\alpha_{1...L}$, $\beta_{1...L}$, $\tau_{x_0,y_0,1...L}$, $\gamma_{x_0,y_0,1...L}$. x_0, y_0 is the point where the measured and the reconstructed CIRs match.

The gains are assumed not to vary a lot within a region. Therefore only the gain values, $\gamma_{x_0,y_0,1...L}$ from the CIR at location x_0, y_0 are required for the CIR generation. The artificially generated CIRs are denoted as $y_{x,y}^{(art)}[n]$ in Figure 3.8.

For both ways next the CIRs are converted to baseband and down sampled by the factor 12 to get close to the Nyquist rate which is 4 GS/s assuming 4 GHz bandwith. After the down sampling each CIR has 125 sampling points. Figure 3.9 and Figure 3.10 show a CIR before and after the post processing.
The mean vector μ and the covariance matrix Σ as the parameters for the fingerprint of a region are now estimated from the measured CIRs $y_{x,y}^{(BB,meas)}[n]$ and from the artificially generated CIRs $y_{x,y}^{(BB,art)}[n]$ respectively.

The empirical covariance matrix (3.5) and mean estimation (3.4) for $R = 28^2$ CIRs is done by a maximum likelihood estimation (MLE) [23].
In addition ray tracing formulas from Chapter 1 were applied to determine the exact delays of each path.

$$\hat{\mu} = \frac{1}{R} \sum_{i=1}^{R} \mathbf{y}_i \tag{3.4}$$

$$\hat{\mathbf{\Sigma}} = \frac{1}{R} \sum_{i=1}^{R} (\mathbf{y}_i - \hat{\mu}_i) (\mathbf{y}_i - \hat{\mu}_i)^H \tag{3.5}$$

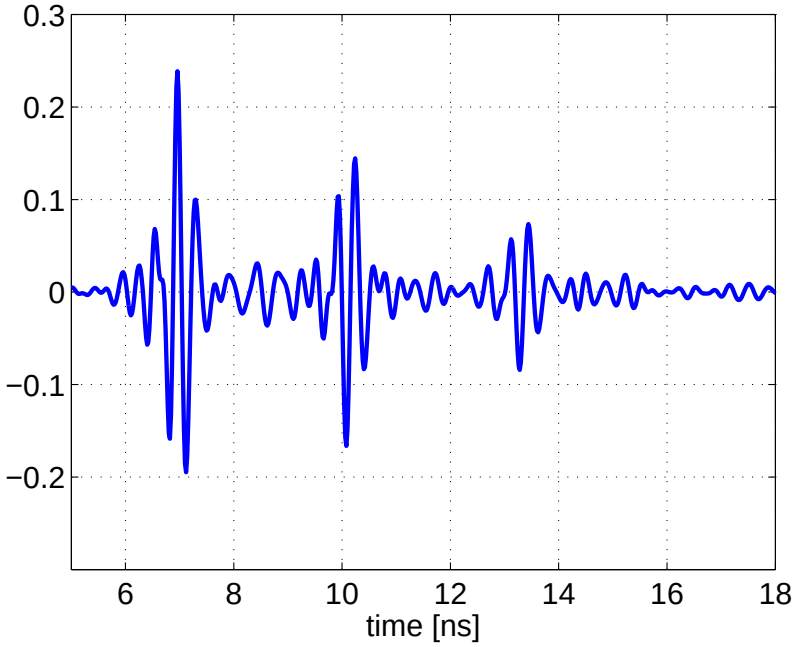

Figure 3.9: CIR of position x_0, y_0 before postprocessing in passband representation

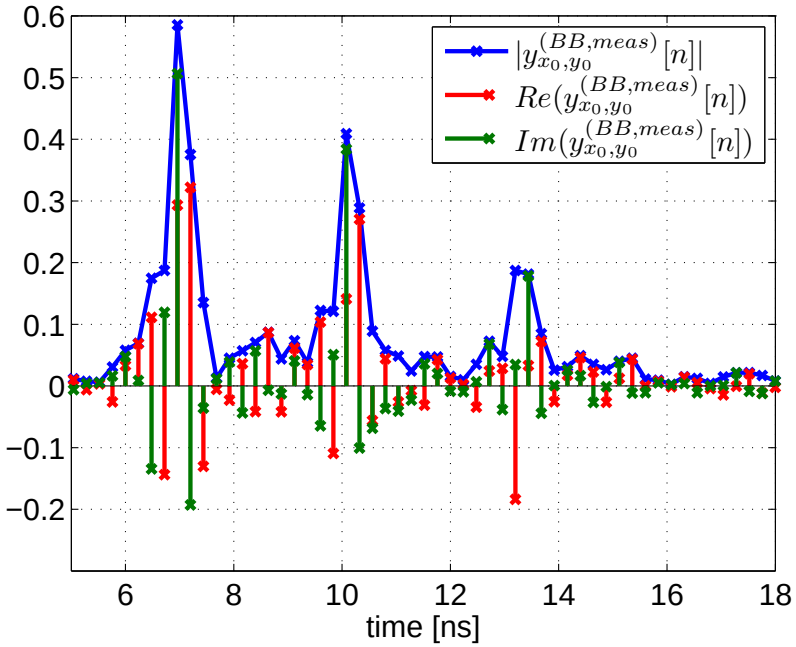

Figure 3.10: CIR of position x_0, y_0 after postprocessing in complex baseband representation

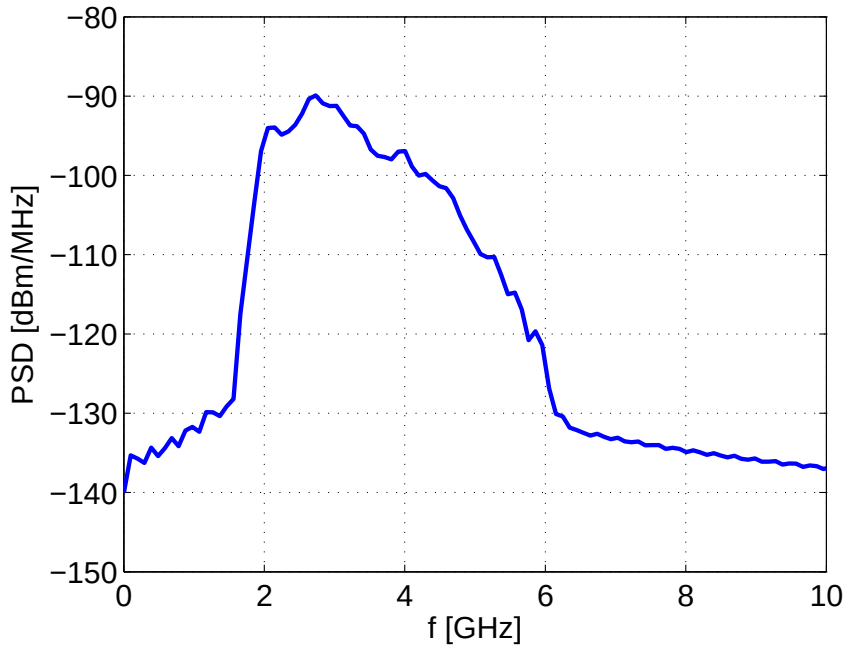

Figure 3.11: Pwelch Power spectral density for the postprocessed CIRs

3.3 Results

Intensity plots of the measured and and artificial CIRs in complex baseband representation for Environment 1 and 2 are shown in Figure 3.12 to 3.15 for the simple and the extended alignment scenario. The corresponding figures for the first environment can be found in Appendix B. It is noticeable the second reflection in Environment 2 does not change its delay over position for the simple alignment scenario because the transmitter is placed orthogonal to the line drawn from transmitter to receiver this effect appears. Such reflections lead to an α or β value of zero.

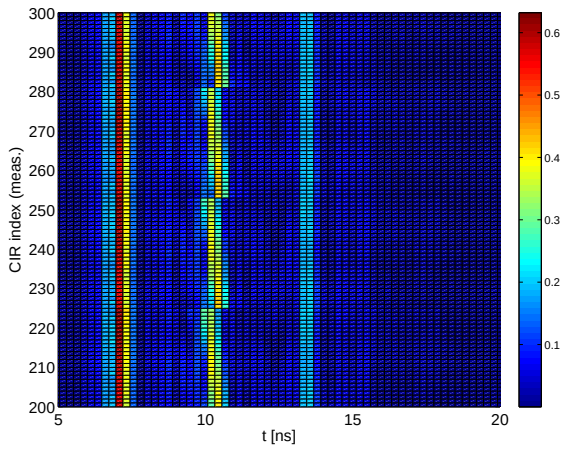

Figure 3.12: 100 measured CIRs (absolute values) with simple alignment for Env. 2

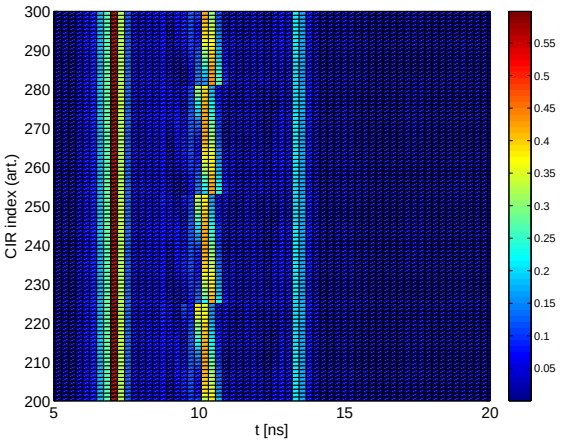

Figure 3.13: 100 artificially generated CIRs (absolute values) with simple alignment for Env. 2

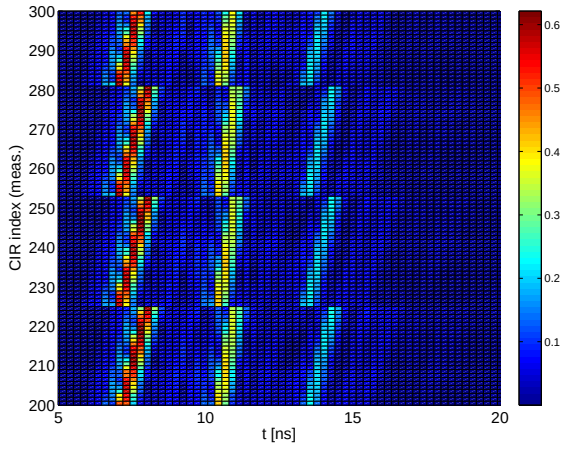

Figure 3.14: 100 measured CIRs (absolute values) with extended alignment for Env. 2

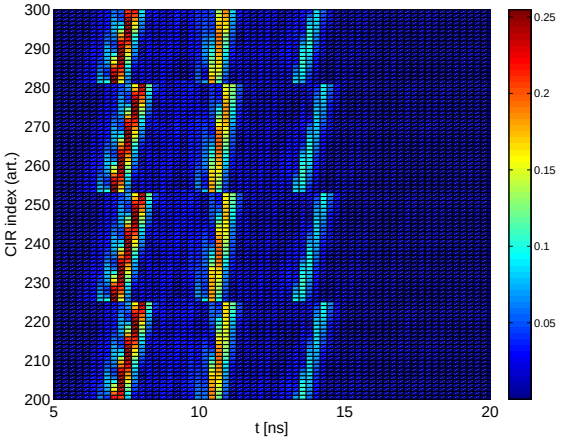

Figure 3.15: 100 artificially generated CIRs (absolute values) with extended alignment for Env. 2

As expected the artificially generated CIRs match the measured CIR best around the reference point x_0, y_0. The farther we move away from the reference point the aberration increases as Figure 3.16 points out.

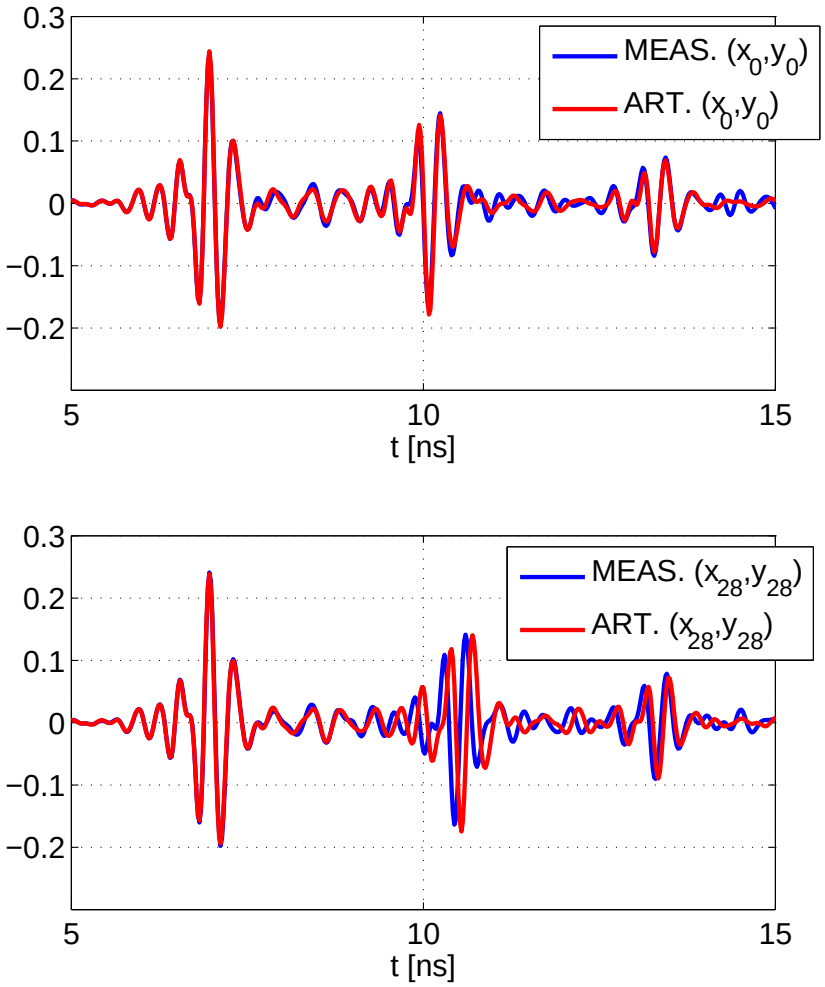

Figure 3.16: Measured and artificial CIR in passband representation for central and outer TX location

The measured and artificially generated CIRs can be arranged in a matrix $\mathbf{Y}$ which has the size of the grid, 28 times 28 and each element is a CIR. A Figure of merit for comparison of the matrix with the measured CIRs $\mathbf{Y}_{meas}$ and the matrix containing the artificially generated CIRs $\mathbf{Y}_{art}$ is the inner product of both. All CIRs are normed to energy of 1. Therefore the inner product is 1 in case of two identical CIRs on both matrices.

The plot displaying the inner product with a Δ of 1 cm (Figure 3.17) shows a faster decay of the inner product values while moving away from the reference point than the

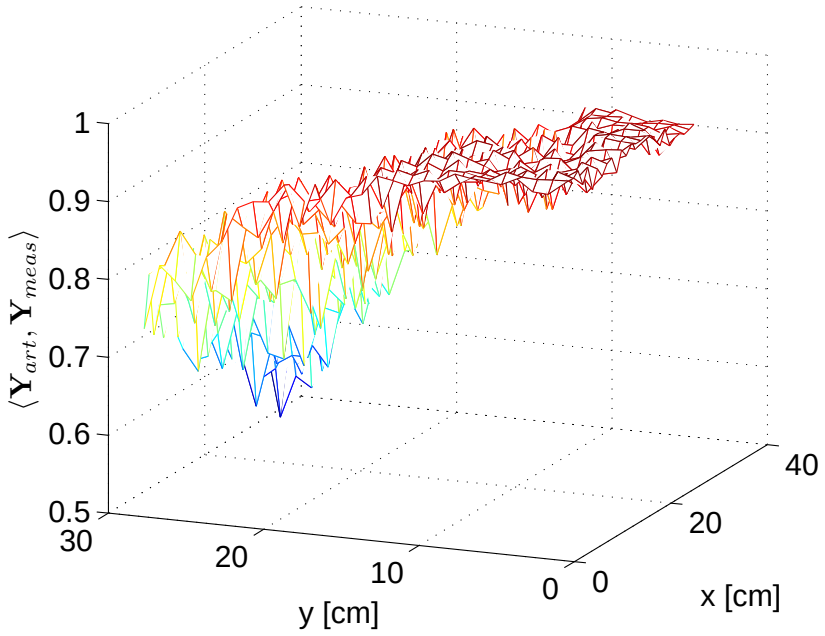

Figure 3.17: Inner product of the matrices with the measured and the artificial CIRs for Env. 2, $\Delta = 1$ cm

plot with the inner product with $\Delta = 27$ cm (Figure 3.18).

Figure 3.19 to 3.22 show surface plots of the second reflection with three planes. The layer with the exact delay values calculated from the geometrical environment is denoted as EXACT, the estimated delay values from the WRELAX algorithm are denoted as WRELAX and the artificial delays reconstructed from the α and β estimation are denoted as ARTIFICIAL.
In point x_0, y_0 the WRELAX and the reconstructed plane match exactly. Its the origin of the reconstruction.
The aberration between the exact and the estimated delays is given on one side by the measurement uncertainty caused while measuring the position of the antennas and the reflectors manually. On the other side by the estimation error of the WRELAX estimator. Due to the high SNR in the anechoic chamber it is possible that the distance measurement error is dominating. Figure 3.21 shows the effect of a small Δ. The artificial delays do not match the measured delays at all. In Figure 3.22 we compensate this drawback by choosing a larger Δ.

From the power delay profiles and the intensity plots of the measured and artificial signatures we see that the delays caused by the first reflector show a significant change of the delay over direction x. Reflections like this are ideal candidates for the α and β estimation.

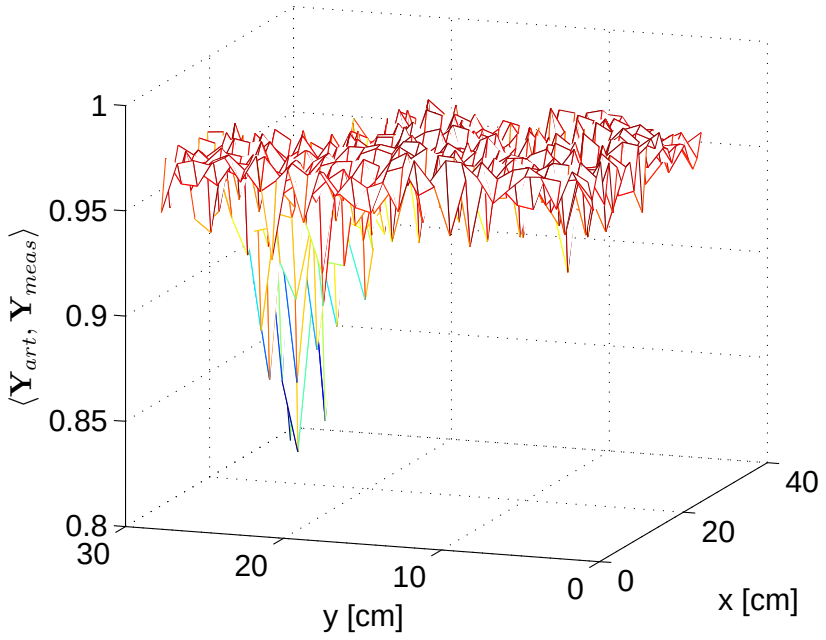

Figure 3.18: Inner product of the matrices with the measured and the artificial CIRs for Env. 2, $\Delta = 27$ cm

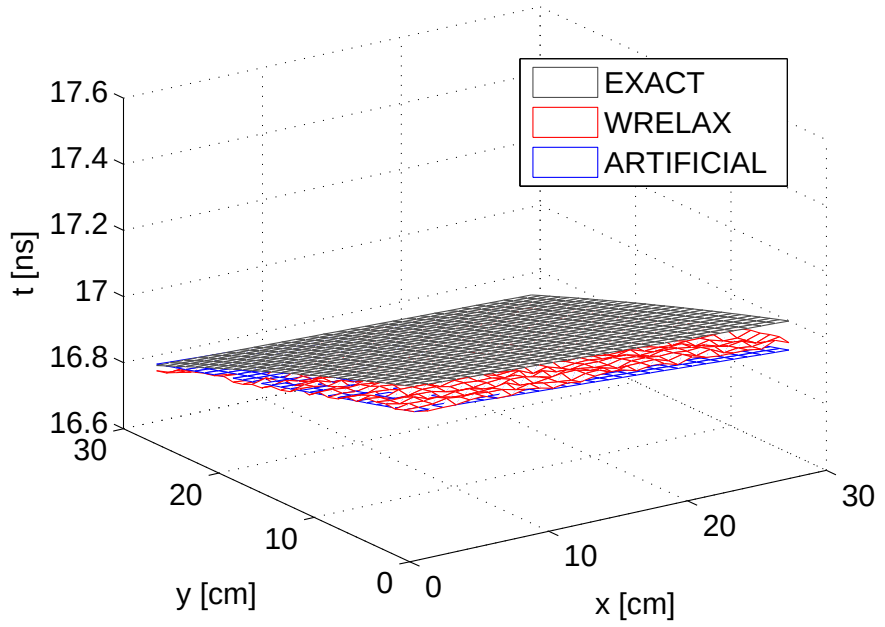

Figure 3.19: Delays of the third reflection in Env. 1 with $\Delta = 1$ cm

Table 3.3 and 3.4 show the results of the estimation for environment 2 using the extended alignment method for two values for Δ. The estimation for the second reflection results in a large error compared to the estimation using the large Δ.

All CIRs from a region are used to estimate the mean vector μ and the covariance

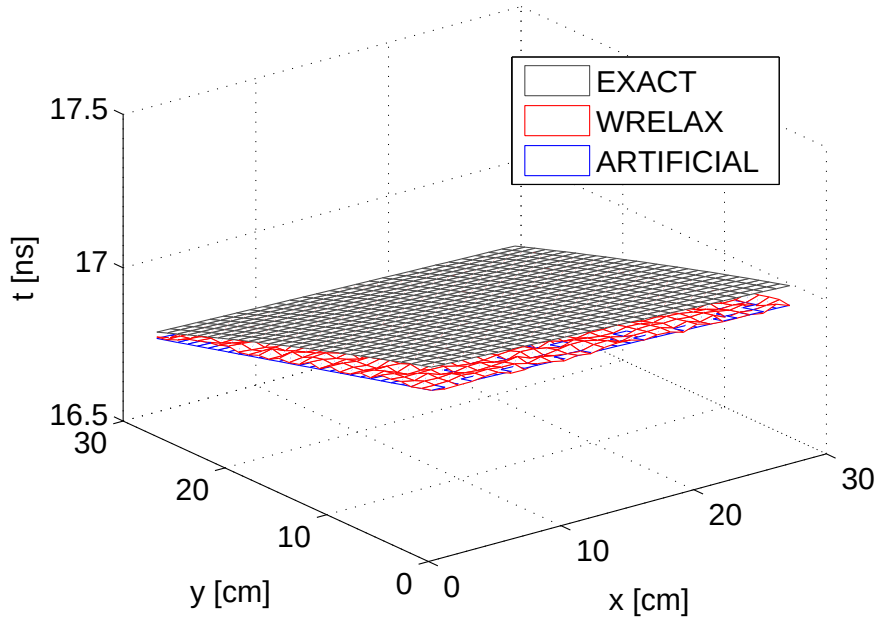

Figure 3.20: Delays of the third reflection in Env. 1 with $\Delta = 27$ cm

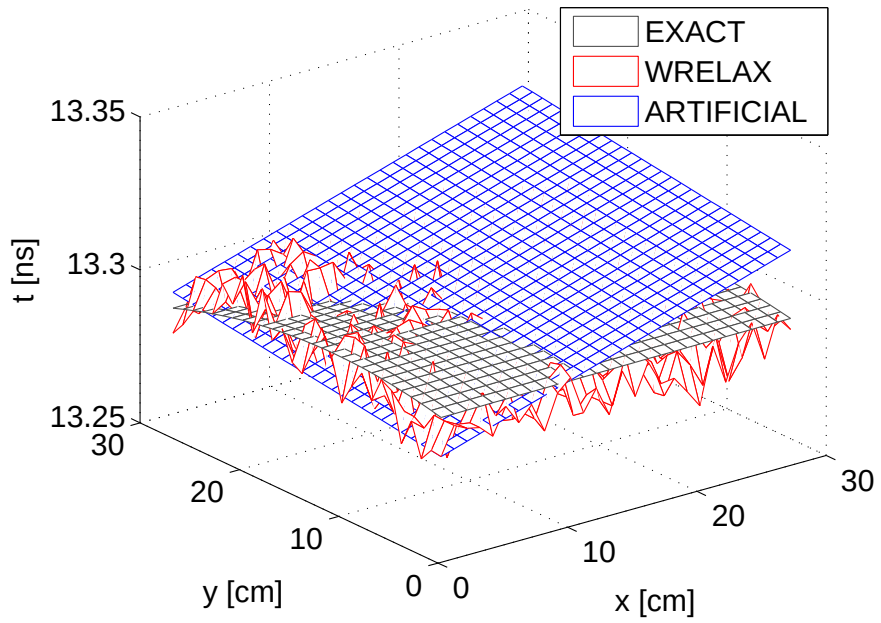

Figure 3.21: Delays of the third reflection in Env. 2 with $\Delta = 1$ cm

matrix $\mathbf{\Sigma}$.

The absolute values of the covariance matrices are shown in Figure 3.27 to 3.30 for the measured and the generated CIRs. The mean vectors for environment one and two are shown in Figure 3.23 and 3.26.

It is notable the mean for the second reflection in the second environment does not reach a

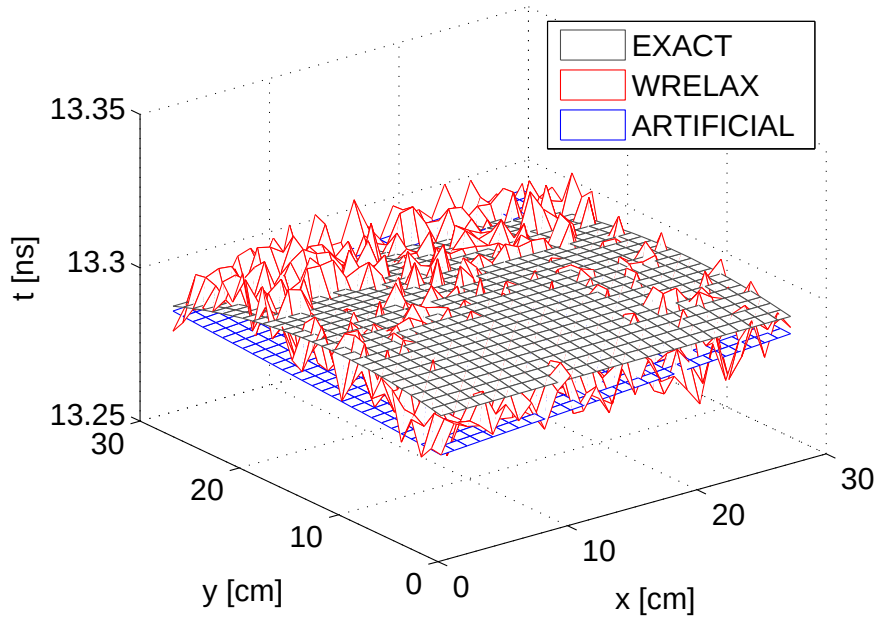

Figure 3.22: Delays of the third reflection in Env. 2 with $\Delta = 27$ cm

value near zero. As mentioned before its because this reflection underlies the same delay variations over space as the LOS path and is therefore eliminated. The second reflection in environment 1 does partially eliminate itself. This occurs because the second reflector is obliquely positioned to the RX antenna.

The mean vector reaches values near zero if we use the extended temporal alignment method as in Figure 3.25 and 3.25.

The values in the covariances from the simulation and from the measurements in the anechoic chamber are mostly around zero which leads to difficulties in calculating the

	$\tau_2 - \tau_1$[ns]	$\tau_3 - \tau_1$[ns]	α_{LOS}	α_1	α_2	β_{LOS}	β_1	β_2
exact	3.36	6.33	-0.05	0.73	-0.03	1.00	0.69	1.00
est.	3.31	6.33	-0.05	0.81	-0.03	1.23	0.87	1.27
diff.	0.05	0.01	0	0.09	0.01	0.23	0.19	0.27

Table 3.3: Results for Env. 2, $\Delta = 1$ cm, extended alignment for grid point x_0, y_0

	$\tau_2 - \tau_1$[ns]	$\tau_3 - \tau_1$[ns]	α_{LOS}	α_1	α_2	β_{LOS}	β_1	β_2
exact	3.36	6.33	0.01	0.75	0.01	1.00	0.71	1.00
est.	3.31	6.33	0.01	0.80	0.01	1.00	0.65	1.01
diff.	0.05	0	0	0.05	0	0	0.06	0.01

Table 3.4: Results for Env. 2, with $\Delta = 27$ cm, extended alignment for grid point x_0, y_0

determinant. A non-zero mean vector leads to less peaks in the covariance matrix. Using the extended alignment method results in a near zero mean vector as shown in Figure 3.26 and 3.25. Due to the subtraction of the mean during the covariance estimation the direct path results in a peak in the covariance matrix at this position as visible in 3.29 and 3.30. The results for the covariance matrices for the second environment can be found in Appendix B. They show a similar behavior.

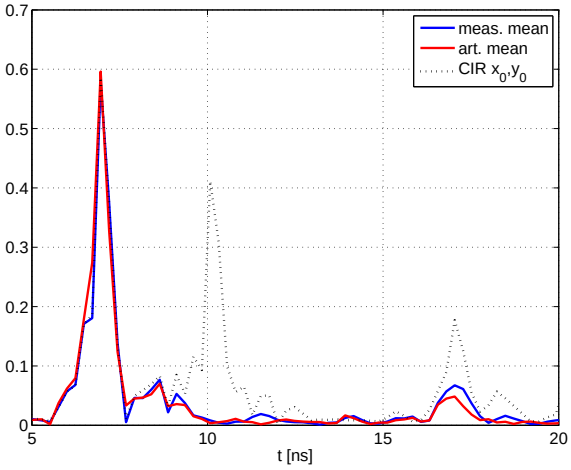

Figure 3.23: Mean vectors for Env. 1 with simple alignment method

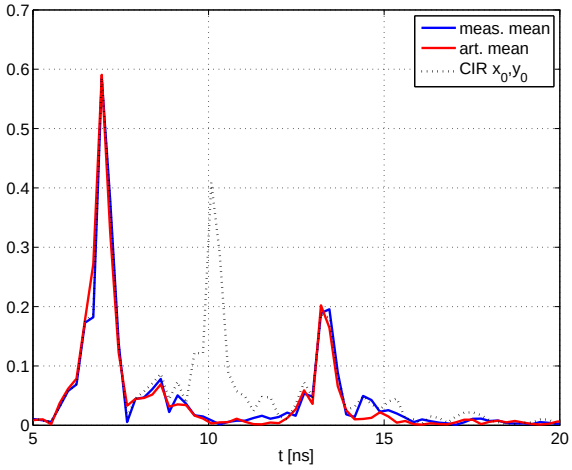

Figure 3.24: Mean vectors for Env. 2 with simple alignment method

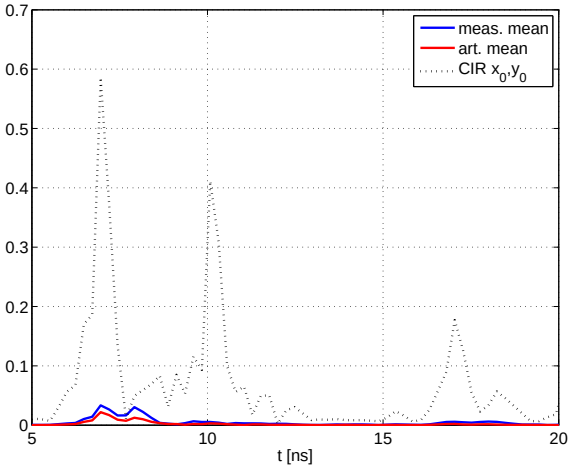

Figure 3.25: Mean vectors for Env. 1 with extended alignment method

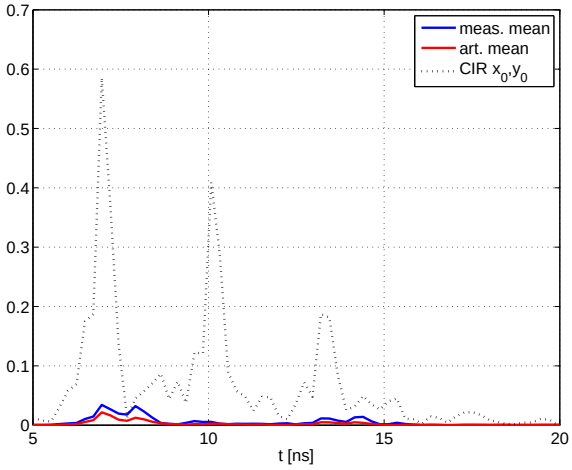

Figure 3.26: Mean vectors for Env. 2 with extended alignment method

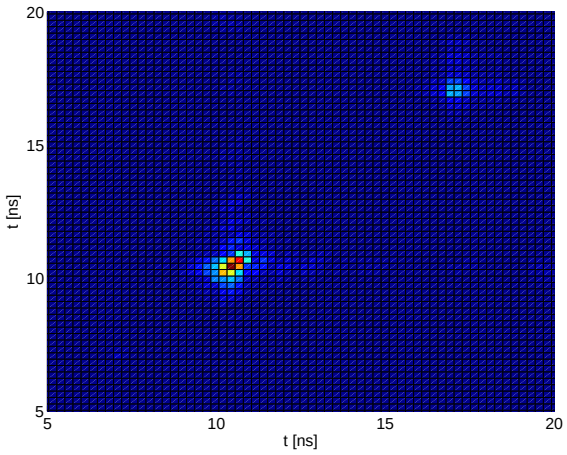

Figure 3.27: Covariance Matrix of Env. 1, estimated from measured CIRs with simple alignment method

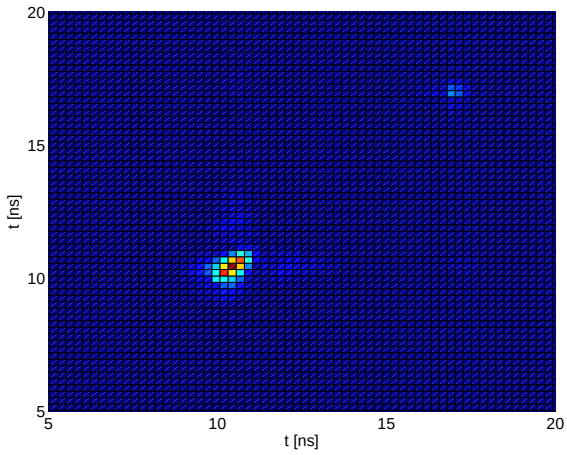

Figure 3.28: Covariance Matrix of Env. 1, estimated from artificial CIRs with simple alignment method

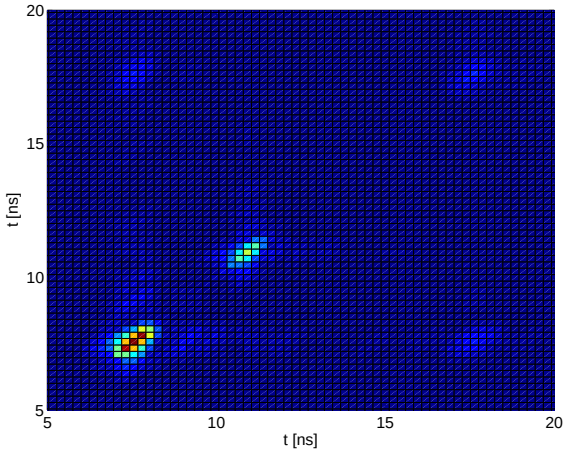

Figure 3.29: Covariance Matrix of Env. 1, estimated from measured CIRs with extended alignment method

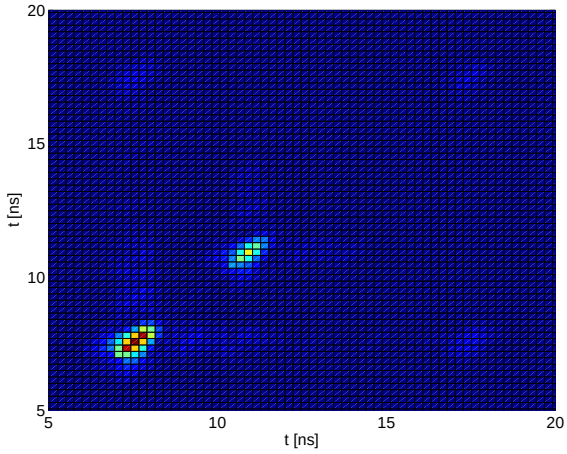

Figure 3.30: Covariance Matrix of Env. 1, estimated from artificial CIRs with extended alignment method

3.4 Conclusion

The AEC campaign with its results was an intermediate step from the pure artificial estimation of the parameters α and β toward the estimation in a real world environment. It is shown that it is possible to reconstruct artificial CIRs which lead to similar fingerprints as the measured CIRs on behalf of the geometry of the propagation environment. The estimated path delays from the measured CIRs accord to the path delays gained from ray tracing with an accuracy around 10^{-2} ns. Not all reflections are suitable in the same way for fingerprint generation.
The selection of the spatial offset Δ is important for an accurate parameter estimation. Larger values for Δ lead to more accurate results.
The temporal alignment procedure has an impact on the mean and furthermore on the fingerprint of a region.

4 Fingerprint Generation from Office Environment Measurements

In this chapter we generate location fingerprints from measurements in an office environment. The measured CIRs are post processed and evaluated in nearly the same fashion as in the previous chapter. The main difference beside the difference of the dense multipath channel is that the CIR signatures were recorded for six regions and the second method for the α and β estimation based on the Hough transform is introduced.

4.1 Motivation

An office environment is an interesting target environment for UWB applications due to its flat spectral mask with low emission rates. Lately the indoor propagation channel including home and office environments gained considerable attention for the UWB technology. Multimedia streaming applications for high definition (HD) contents were deployed under the label 'Laptop to HD' including the wireless HDMI standard based on UWB technology [15]. Wireless docking solutions used as the interface between laptops with peripheral devices in some cases using the wireless USB standard [40].
The main goal of this office environment campaign is it to find out, if its possible to generate reliable fingerprints using our methods of CIR reconstruction presented in Chapter 1.

4.2 OEV Measurement Campaign

The room used for the office environment campaign was the RF-Laboratory on floor E in the ETF building of ETH Zürich. A map of the room is shown in Figure 4.1.

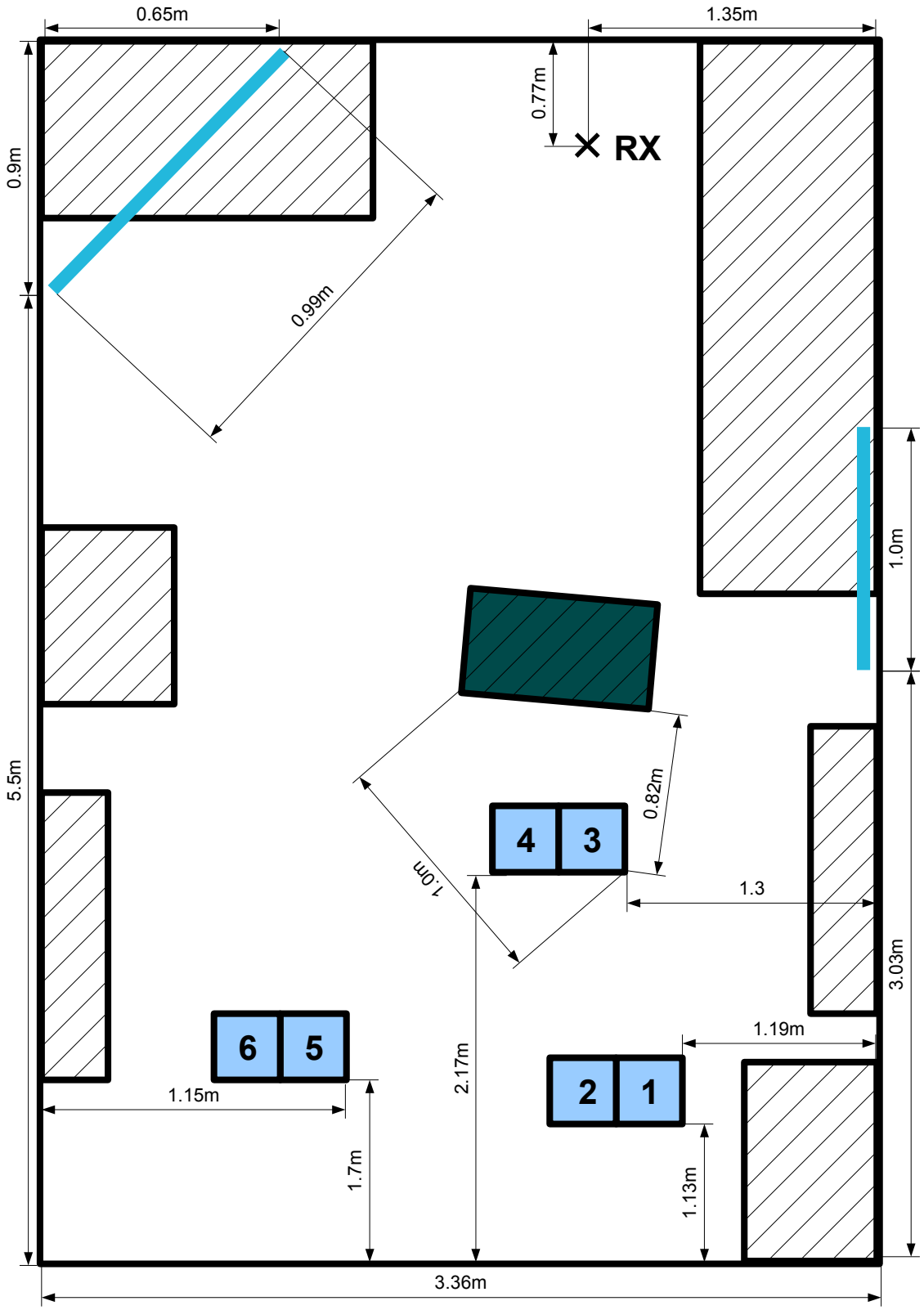

Figure 4.1: Office Environment floor plan

To obtain adequate values for the parameters α and β we need paths which are well traceable over space. To enforce this condition we placed artificial reflectors in the room. One in the middle of the right wall and another one in the upper left corner as shown on the floor plan (see 4.1). Six regions were selected in a manner such that every region reaches both artificial reflectors. Each region has a size of 28 times 28 cm with a grid spacing of 1 cm. The same positioning device as in the previous campaign from Chapter 3 was used to move around the TX antenna on the grid in each region.
The box in front of Region 3 and 4 is only used for the NLOS scenarios and is not present in all other scenarios.
The measurement parameters and components are the same as in the campaign in the anechoic chamber (see Chapter 2).

4.2.1 Measurement Setup

The setup for this campaign is the same as used in the previous campaign in the anechoic chamber shown in Figure 3.2. During this campaign the preamplifier was used in every scenario. Parameters for the office environment are listed in Table 4.1.

Parameter	Value
Sampling Rate	50 GS/s
Horizontal resolution	1 μs/div
Vertical resolution	300 mV/div
Antenna height	1.69 m
PN Clock rate	8 GHz
PN Order	15
PN Sequence duration	$(2^N - 1)\frac{1}{8GHz} \approx 4.1\mu s$
PAMP Gain	30 dB
PAMP Bandwith	2 - 8GHz
PAMP Power	30 dBm
Highpass	Loss: under 1dB over 910 MHz

Table 4.1: Office Environment Measurement Parameters

4.2.2 Measurement Scenario

The campaign was subdivided into the following scenarios:

- Scenario 1: Principal setup without reflectors, without positioning device

- Scenario 2: Positioning device without reflectors
  1. Region 1 to 6 LOS
  2. Region 3,4 NLOS
- Scenario 3: Positioning device with reflectors
  1. Region 1 to 6 LOS
  2. Region 3,4 NLOS

The goal of the first scenario was to reconstruct the measurement setup as it was in the first campaign. The base pulse $y_B[n]$ without reflection captured in the anechoic chamber is formed by the transfer functions of our components and is very sensitive to changes in the setup. The WRELAX algorithm which we use to extract gains and delays from the captured impulse responses requires a base pulse which fits our measurements. Therefore the LOS component of both campaigns had to be the same.
After the principal setup we performed scenario 2 without reflectors and scenario 3 with reflectors. The positioning device was set onto the six regions one after the other. For regions 3 and 4 in addition RF absorber material (the green box in Figure 4.1 was placed in front of the antenna in order to obtain a NLOS situation. The estimated spectra of the measurements is shown in Figure 4.3. In total $784 \times 2 \times 6 + 784 \times 2 \times 2 = 12544$ CIRs were recorded. Figure 4.2 shows the basepulse from the anechoich chamber and a typical line of sight CIR measurement from the office environment in passband represenation. Both are normed to an energy of one.

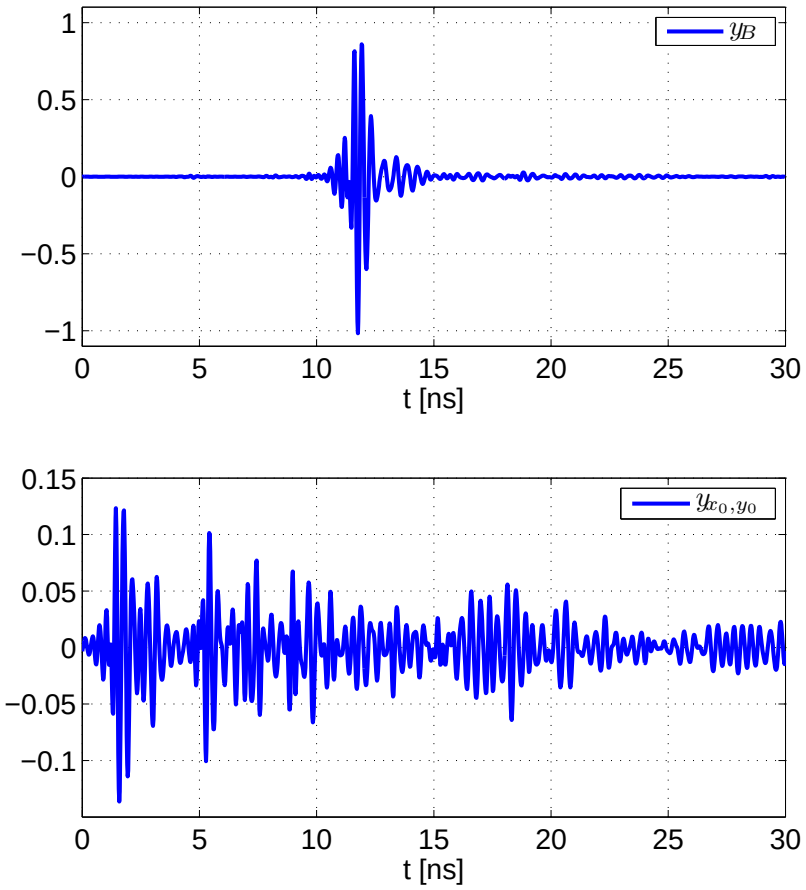

Figure 4.2: Basepulse y_B and a typical CIR from the office environment in passband

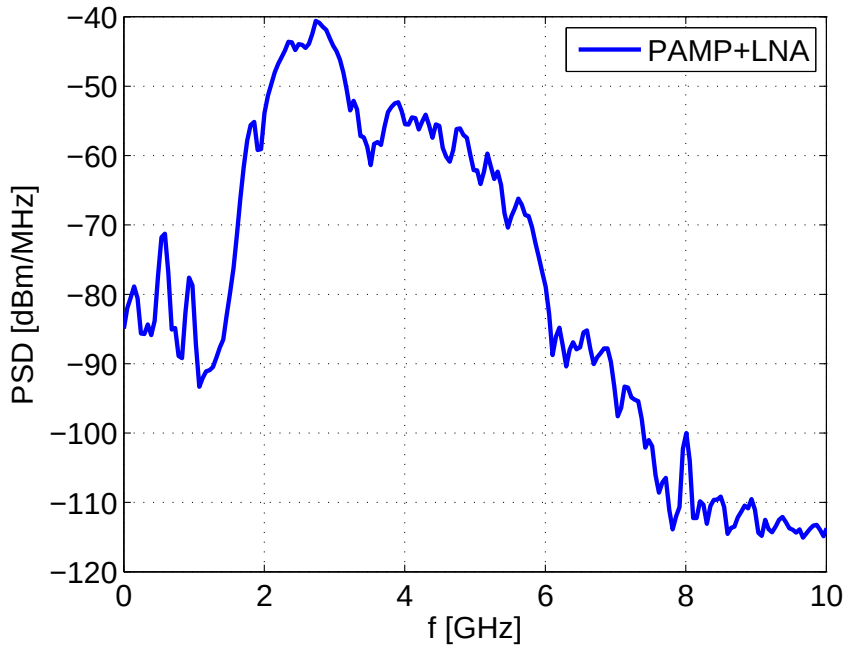

Figure 4.3: PSD of a single CIR measurement from the office environent

4.3 Postprocessing

The post processing procedure is basically the same as for the AEC campaign explained in Chapter 3 with some differences.
We align all CIRs to a reference sample. The seventh channel tap of the time vector is chosen as the reference sample. For the LOS measurements we assume the first path is the direct path and samples before the first paths are negligible. For the NLOS measurements we align the first sample which reaches 20% of the maximum amplitude to the reference sample.
The goal of the α and β estimation is to find the course of a path delay over space in a region. We refer to to this search as spatial delay tracing/tracking. For this campaign we investigated and implemented two ways. The first way is the same as in the AEC campaign using three CIR measurements. The second way is a more elaborate method based on the Hough transform.
Another difference is the parameter L representing the number of paths to estimate. For the AEC campaign choosing L was obvious. In the OEV campaign estimations were made with three different values for L ($L \in \{12, 15, 20\}$).

4.3.1 Region Cropping

The size of a region is an important parameter for the artificial generation of CIRs. Therefore we cropped our measured regions with width $W = 28$ into smaller regions with $W \in \{4, 6, 12\}$. The cropping is done in a manner that the cropped regions are still neighbor regions as shown in Figure 4.4.

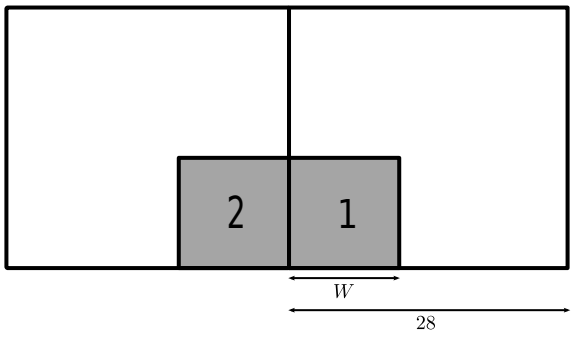

Figure 4.4: Region Cropping

4.3.2 Spatial delay tracking based on the Hough Transform

The Hough transform, in it's classical version is used to find lines in images. Later it was extended to find positions of arbitrary figures [10]. Remember that α and β represent

inclinations of path delays over a spatial direction. If we look at a representation of the delays of a CIR over W points in a region as shown in Figure 4.5 it is obvious the Hough transform can be helpful. With the Hough transform we can find lines in the delay picture. The inclinations of those lines determine the values of the parameters α or β. The points along the line are the estimated delays $\hat{\tau}_l$.

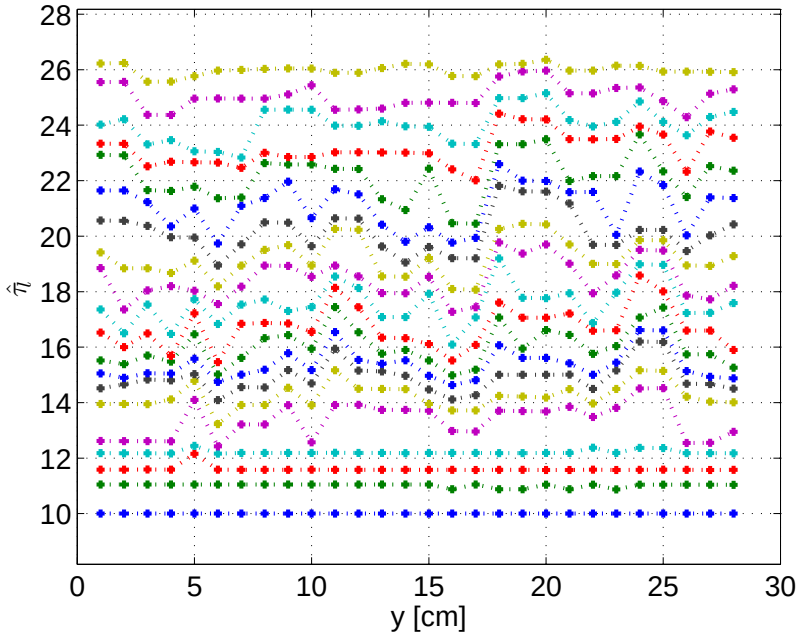

Figure 4.5: Delay Picture of region 4, delays in ns

The lines we want to find in the delay picture are characterized by two parameters, the inclination α or β and the offset $\tau_l(x_0, y_0)$.

$$\hat{\tau}_l(x, y_0) = \alpha_l(x_0 - x) + \tau_l(x_0, y_0) \tag{4.1}$$

$$\hat{\tau}_l(x_0, y) = \beta_l(y_0 - y) + \tau_l(x_0, y_0) \tag{4.2}$$

The Hough transform in its traditional implementation uses the parameters Θ and r to characterize a line. There a line is written as in (4.3) derived from (4.4) where r is the distance between the origin of the coordinate system and the line and Θ is the angle between the horizontal axis and r within the range 0 to π. Figure 4.6 shows this relationship.

$$y = \left(-\frac{\cos\Theta}{\sin\Theta}\right) x + \left(\frac{r}{\sin\Theta}\right) \tag{4.3}$$

$$r = x \cos\Theta + y \sin\Theta \tag{4.4}$$

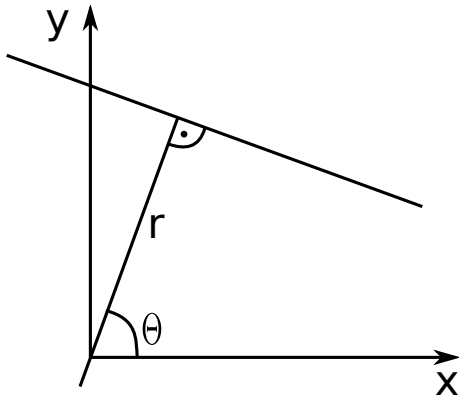

Figure 4.6: Hough transform concept in general

The distance to the origin is of minor importance for our case because the distance of each delay-line l is given by $\tau_l(x_0, y_0)$. Hence we only have to estimate one parameter, the α_l or β_l. The picture containing the delay points (Figure 4.5) has the size W times L. For each delay line $l = 1 \ldots L$ we draw lines with the point $\tau_l(x_0, y_0)$ as origin and certain angles into the picture. For each line we prove with how many points from the delay line our line intersects within a threshold t_{th}. The line which intersects with the most points has the inclination of the wanted α or β. Figure 4.7 illustrates this principle.

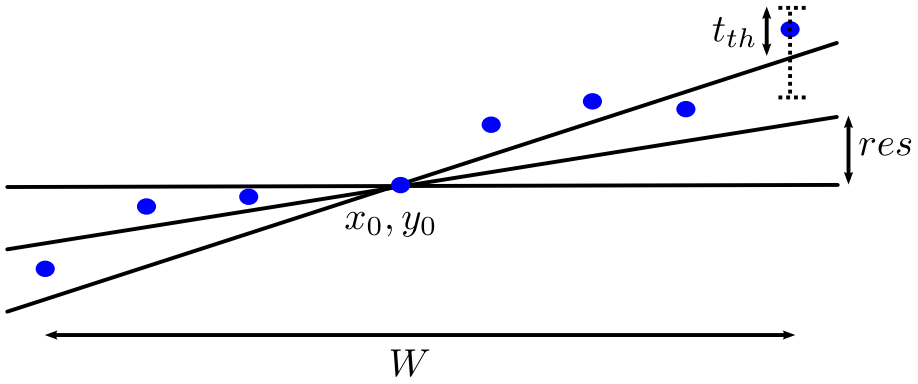

Figure 4.7: Hough Transform concept applied on path delays

This estimation procedure has two parameters which determine computational load and accuracy. The resolution of the inclination of the lines and the threshold for the intersection. The inclination reaches from -2 to 2. 0.1 for the resolution and 0.05 ns for the threshold t_{th} are good choices in our case.

4.3.3 Generation of exact values

For comparison of the α and β values gained from the estimation procedures with exact values we measured the office environment using a tape measure. From the knowledge of the geometry we calculated the exact CIRs via ray tracing and the α and β values as shown in 4.8 for the following eight reflectors:

- Floor
- Ceiling
- 4 Walls
- 1st reflector (if used)
- 2nd reflector (if used)

L' denotes the amount of exact reflection paths considered.

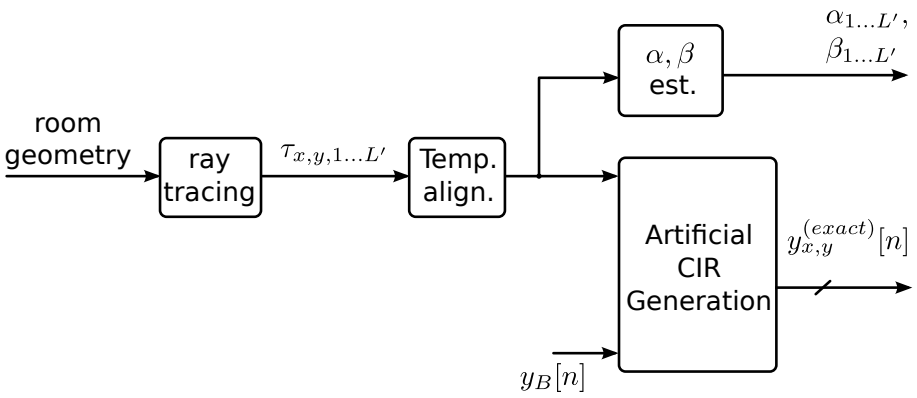

Figure 4.8: Generation of exact values

4.4 Results

In this section, we will investigate and compare three types of results:

- Measured CIRs with fingerprints
- Artificially reconstructed CIRs from α and β estimation with fingerprints
- Exact CIRs and α and β, generated from the delays calculated from the room geometry by using ray tracing

The following evaluations use region 3 as transmit region, with reflectors in the environment and $(x_{\lceil W/2 \rceil}, y_{\lceil W/2 \rceil})$ as reference CIR position (x_0, y_0) on the region grid. The covariance matrices are estimated using the MLE estimator (3.5) with zero mean vectors. The zero mean assumption is justified because the CIRs are averaged over different transmitter locations and due to constructive and destructive interference the multipath components are eliminated [33].

4.4.1 CIR reconstruction

In general the reconstruction of the CIRs on behalf of the α and β values works for grid positions not distant from the reference location. This holds for the Hough transformation based reconstruction as well as for the reconstruction based on 3 measurements. Hence the quality of reconstruction with our method strongly depends on the region size. We can observe this effect if we compare Figure 4.9 and Figure 4.10. The region from Figure 4.9 has a width of 6 cm while the region in Figure 4.10 has a width of 28 cm. The aberration between the artificially generated and the measured CIR is higher in the larger region.
This effect is based on our initial assumption that the gains do not vary in the order of the carrier wavelength. For our spectrum the carrier wavelength is 6.67 cm.
An adequate figure of merit for the reconstruction quality is the inner product between the measured CIRs and the artificially generated CIRs as introduced in Chapter 3. The inner product of the region with width $W = 6$ is shown in Figure 4.11 and the product of the region with width $W = 28$ is shown in Figure 4.12. The mentioned Figure shows the inner product built with the artificial CIRs from the Hough transform and with the α and β estimation based on 3 CIR measurements. The CIRs of the large region show a peaked shape and inner product with a steep decay when moving away from the reference CIR in the middle of the grid. The small regions inner product from Figure 4.11 is relatively flat. The CIRs generated with the α and β from the Hough transform show a slightly better reconstruction. The inner product values are higher on most grid points.

Two examples of the CIRs generated from the exact delays based on the room geometry together with the measured CIRs are displayed in Figure 4.14. The arrows accord to those in Figure 4.13. Note (1) in the Figure points to reflections not covered by the exact CIRs. They result from objects near the RX antenna including desk, stative and oscilloscope. The reflection from the behind the RX antenna is labeled with (2). It has however worse reflection properties than a plain wall. Path at note (3) is reflected from the floor and corresponds with the path in the measured CIR. The reflections at note (4) are close reflected from the wall and the reflector on the right side. The strong path at note (5) comes from the wall behind the RX antenna. On this position there is a window

in the wall. The window was closed with closed roller blinds. The roller blinds are made from aluminum and represent a big reflection area. The path from the second reflector in the left corner is marked with note (6). The last path is caused by the reflection from the wall behind the TX antenna.

Figure 4.13 shows the eight α values calculated from the geometrical dimensions denoted as EXACT and the 15 estimated α values resulting from the Hough transform denoted as HOUGH. In the case of our environment the α values are more significant because the x direction points from the RX to the TX antenna. We see that only a part of the red lines match the black ones within a certain threshold.

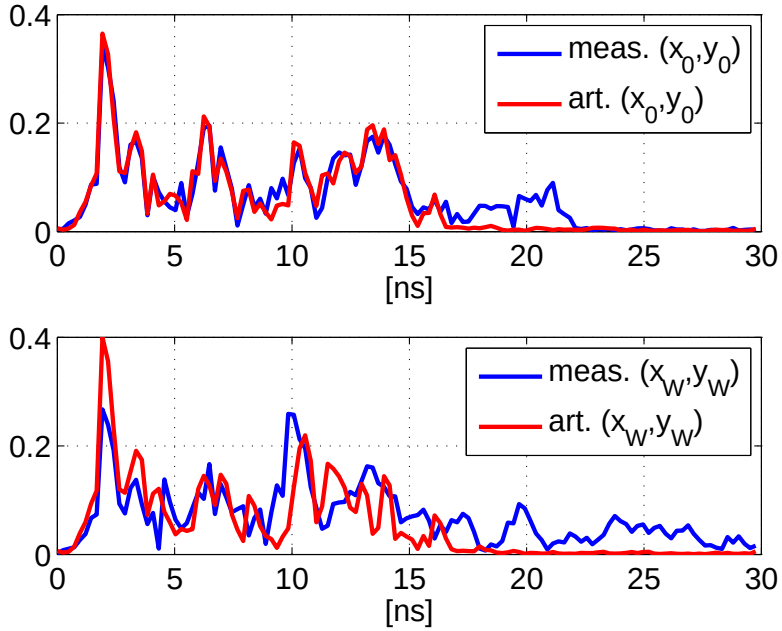

Figure 4.9: Envelope of measured and reconstructed CIRs using the Hough transform for region 2 with $W = 6$ and $L = 12$ for central and outer position on the grid

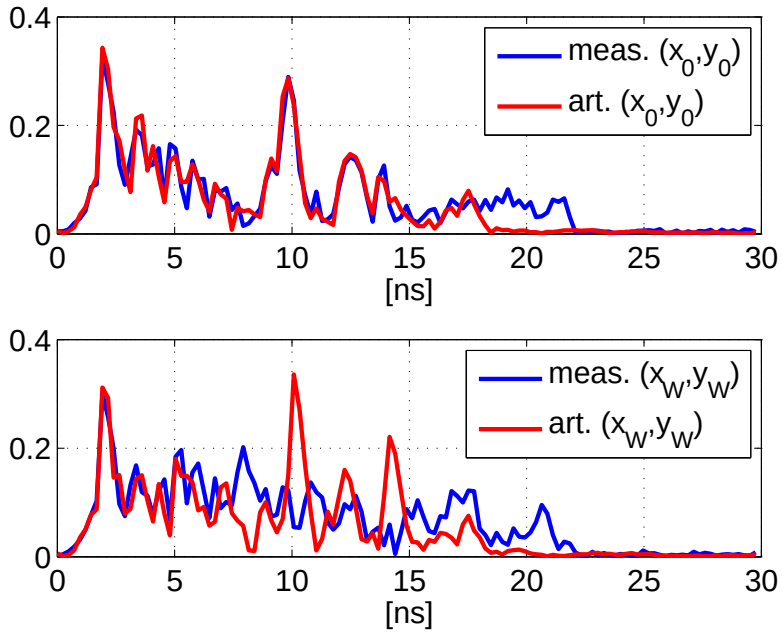

Figure 4.10: Envelope of measured and reconstructed CIRs using the Hough transform for region 2 with $W = 28$ and $L = 12$ for central and outer position on the grid

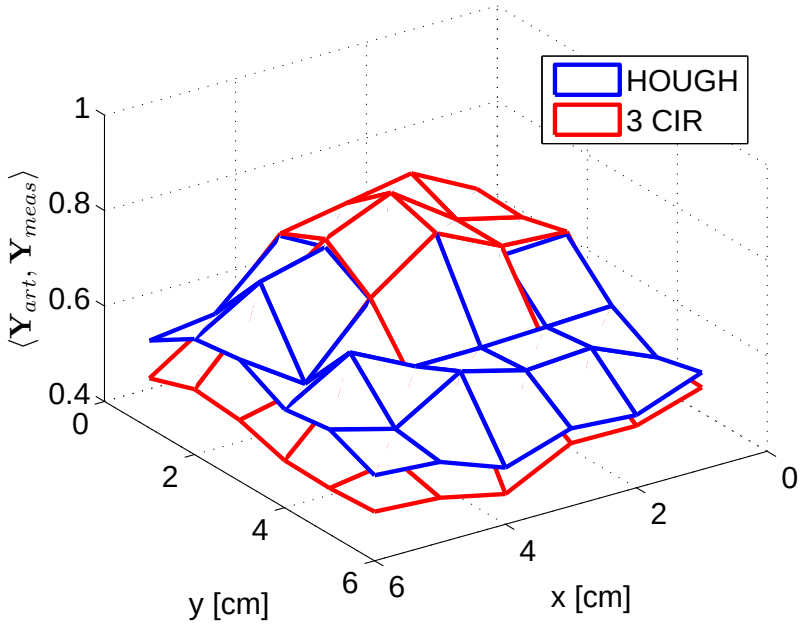

Figure 4.11: Inner product of measured and art. generated CIRs, $W = 6$ and $L = 20$

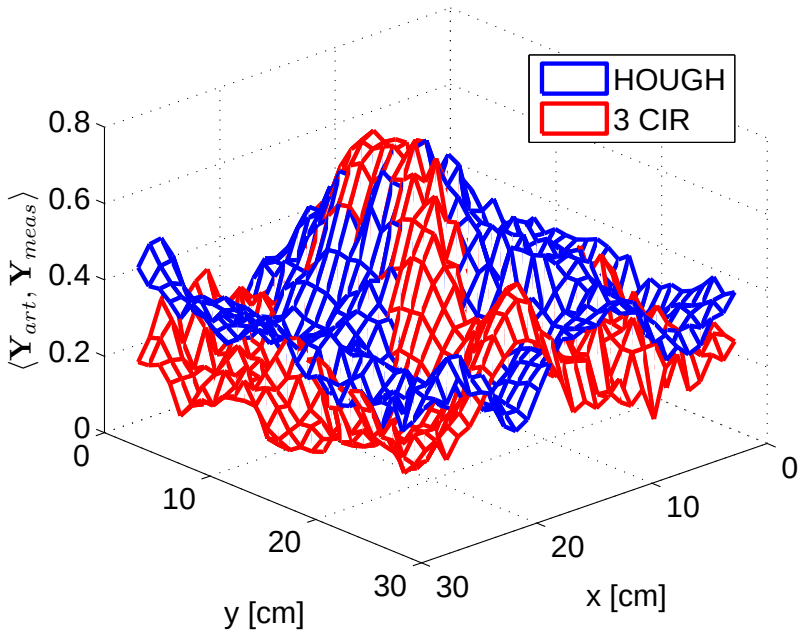

Figure 4.12: Inner product of measured and art. generated CIRs, $W = 28$ and $L = 20$

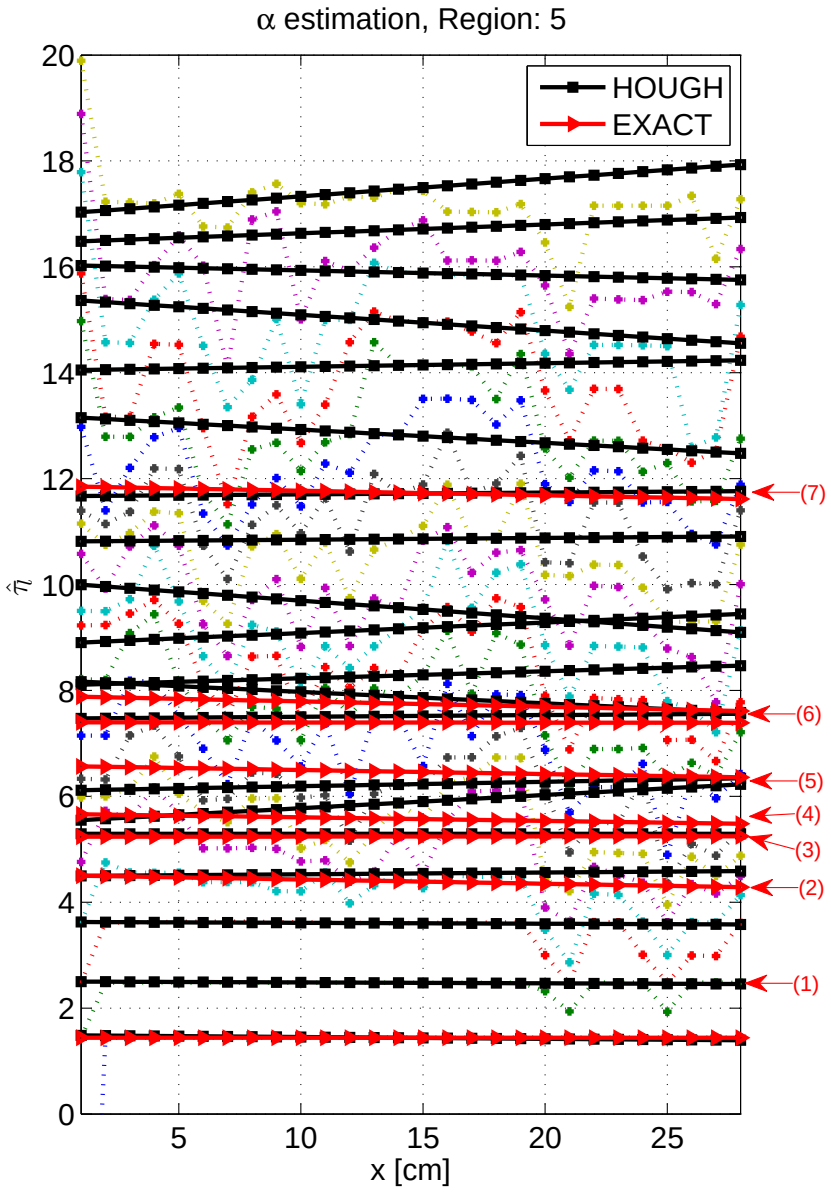

Figure 4.13: Exact and estimated delays for region 5 using $W = 28$ and $L = 20$

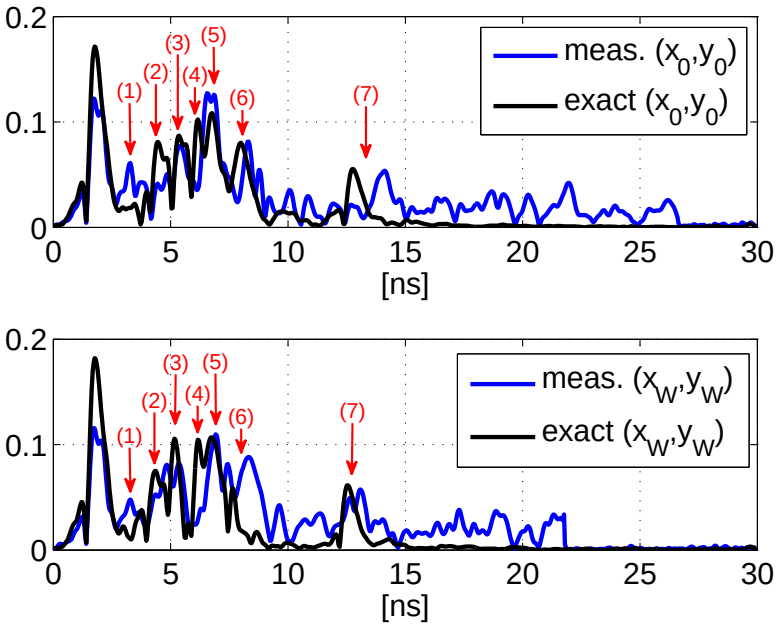

Figure 4.14: Envelope of measured and "exact" CIRs for region 5 with $W = 6$ and $L = 20$ for central and outer position on the grid

4.4.2 Mean vectors and covariance matrices

The imperfect reconstruction leads to differences in the parameters used for fingerprint modeling.

For large regions the mean vector is lower than for smaller regions because of small delay variations paths do not eliminate themself by averaging.

The absolute values of the covariance matrices are shown in Figure 4.17 to 4.20. The fact that we gain a better reconstruction for smaller regions results also in the covariance estimation. The measured and the artificially generated covariance matrix for the region with width $w = 6$ look very similar (Figure 4.17 and 4.18) while the covariance matrices for the region with width $W = 28$ look obviously different (Figure 4.19 and 4.20). The generated means and covariance matrices were reconstructed based on the Hough transform. The covariance matrices reconstructed with the simple method look similar and can be found in Appendix C.

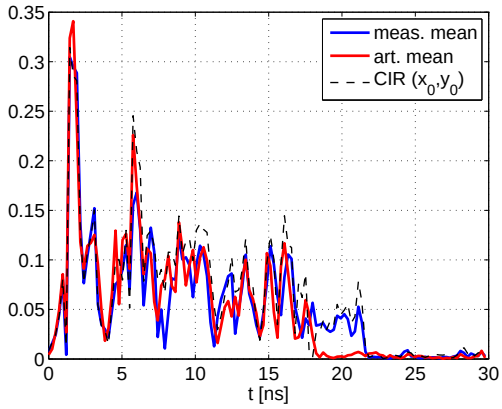

Figure 4.15: Mean vectors for region 3, $W = 6$, $L = 12$

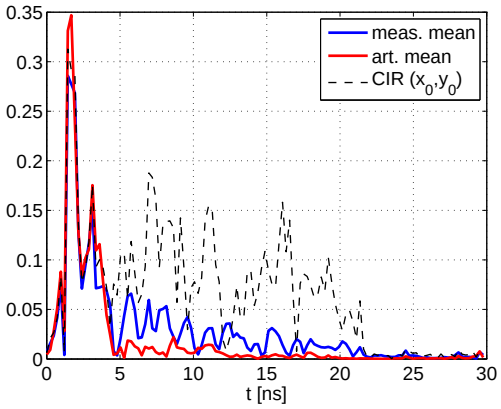

Figure 4.16: Mean vectors for region 3, $W = 28$, $L = 12$

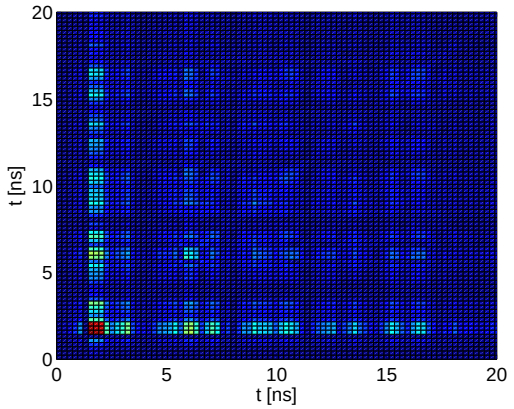

Figure 4.17: Covariance Matrix of region 3, estimated from measured CIRs, $W = 6$

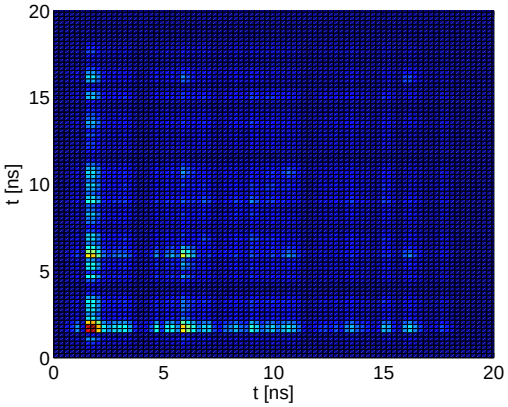

Figure 4.18: Covariance Matrix of region 3, estimated from art. generated CIRs, $W = 6$

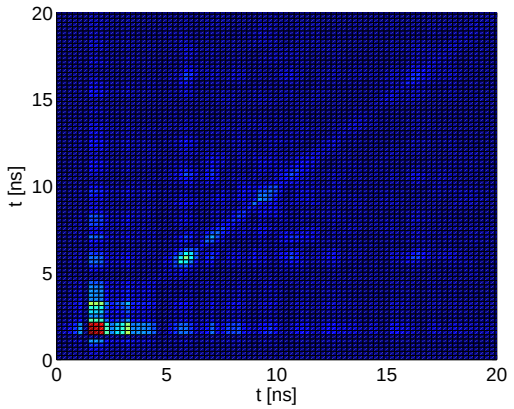

Figure 4.19: Covariance Matrix of region 3, estimated from measured CIRs, $W = 28$

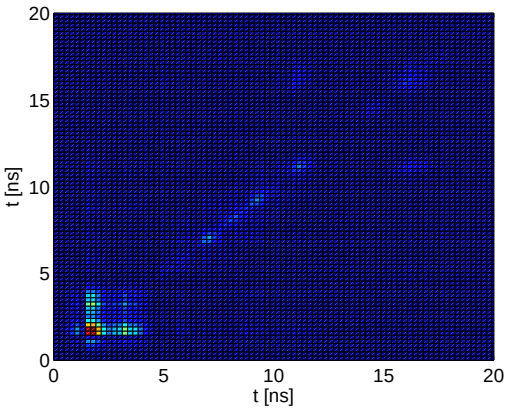

Figure 4.20: Covariance Matrix of region 3, estimated from art. generated CIRs, $W = 28$

4.5 Conclusion

In the office environment the reconstruction process is way more difficult than in the anechoic chamber (Chapter 3). The delays show a strong variation over space in all directions for the LOS and for the NLOS measurements.
Anyhow path delays calculated with ray tracing roughly accord to the measured and artificially generated paths.
No performance difference was detected between LOS and NLOS measurements. For large regions it is not possible to reconstruct CIRs on behalf of the α and β estimation. Neither with the Hough transform nor with the estimation from 3 CIR measurements. The spatial path tracking based on the Hough transform fails, because the path gains vary too much over both directions. Using smaller regions we gain feasible results for the reconstruction. A width of 6 cm for a region seems to be a good choice. The placement of additional two reflectors in the environment did not lead to any measurable differences. As well the reconstruction did not show a significant performance variance while changing the number of paths to estimate $L \in \{12, 15, 20\}$.

5 Performance Evaluation of Office Environment Location Fingerprinting

The goal of the location fingerprinting system is to detect the region a transmitting node is currently located. A location fingerprinting algorithm as presented in [34] is explained to evaluate the performance. Results in terms of error probabilities P_e and average positioning error d_e are presented for different settings.

5.1 Position Location as a Hypothesis Testing Problem

Each region with width W contains W^2 realizations of the random vector describing a CIR. Those realizations are used to estimate the mean vector $\hat{\mu}$ and the covariance matrix $\hat{\mathbf{\Sigma}}$ for each region. $\hat{\mu}$ and $\hat{\mathbf{\Sigma}}$ are used to model the probability density of a CIR being transmitted from the corresponding region. We assume $\mathbf{y}$ is a received CIR transmitted from an unknown region.

5.1.1 Binary Hypothesis Testing

For the binary case we have two possible hypothesis A and B. Hypothesis A indicates the transmitter exiting $\mathbf{y}$ is located in region A, while hypothesis B indicated the transmitter exciting $\mathbf{y}$ is located in region B. $\hat{\mu}_A$ and $\hat{\mathbf{\Sigma}}_A$ denote the mean vector the covariance matrix estimated from the CIRs from region A.
The probability density for region A as transmit region is denoted as $p(\mathbf{y}|A) = \mathcal{CN}(\hat{\mu}_A, \hat{\mathbf{\Sigma}}_A)$. and the according binary hypothesis test with equal a priority probabilities for both hypotheisis is written in (5.1).

$$p(\mathbf{y}|A) \underset{B}{\overset{A}{\gtrless}} p(\mathbf{y}|B) \tag{5.1}$$

For the complex Gaussian probability densities defined in (1.3) we obtain the decision rule (5.2). This hypothesis test uses the estimated covariance matrix and mean vector and is referred as COV approach.

$$(\mathbf{y}-\hat{\mu}_B)^H\hat{\mathbf{\Sigma}}_B^{-1}(\mathbf{y}-\hat{\mu}_B)-(\mathbf{y}-\hat{\mu}_A)^H\hat{\mathbf{\Sigma}}_A^{-1}(\mathbf{y}-\hat{\mu}_A)\underset{B}{\overset{A}{\gtrless}}\ln\left(\frac{|\hat{\mathbf{\Sigma}}_A|}{|\hat{\mathbf{\Sigma}}_B|}\right) \tag{5.2}$$

If we assume zero mean for our CIRs we obtain (5.6).

$$\mathbf{y}^H\left(\hat{\mathbf{\Sigma}}_B^{-1}-\hat{\mathbf{\Sigma}}_A^{-1}\right)\mathbf{y}\underset{B}{\overset{A}{\gtrless}}\ln\left(\frac{|\hat{\mathbf{\Sigma}}_A|}{|\hat{\mathbf{\Sigma}}_B|}\right) \tag{5.3}$$

The second approach we investigated considers the average power delay profile (referred as PDP approach) of the CIRs as defined in (5.4). Only the diagonal of the covariance matrix $\hat{\mathbf{\Sigma}}$ is used.

$$APDP[n]=\frac{1}{R}\sum_{m=1}^{R}|y_m[n]|^2=\hat{\mathbf{\Sigma}}[n,n] \tag{5.4}$$

This approach assumes the channel taps are independent and leads to worse performance results as the first approach [33]. For the PDP approach we can find the decision rule written in (5.5).

$$\sum_{n=1}^{K}\left(\frac{(y[n]-\mu_A[n])^2}{APDP_A[n]}-\frac{(y[n]-\mu_B[n])^2}{APDP_B[n]}\right)\underset{B}{\overset{A}{\gtrless}}\sum_{n=1}^{K}\ln\left(\frac{APDP_A[n]}{APDP_B[n]}\right) \tag{5.5}$$

If we assume zero mean for our CIRs we obtain (5.6).

$$\sum_{n=1}^{K}|y[n]|^2\left(APDP_A^{-1}[n]-APDP_B[n]^{-1}\right)\underset{B}{\overset{A}{\gtrless}}\sum_{n=1}^{K}\ln\left(\frac{APDP_A[n]}{APDP_B[n]}\right) \tag{5.6}$$

5.1.2 Multiple Independent Observations

We consider multiple CIR observations transmitted from a region. Multiple observations can be emitted from separate antennas sequentially or from one antenna over different positions within a region [34]. The total number of observations is denoted by K.

5.1.3 M-ary Hypothesis Testing

The previous section investigated the performance for two regions. To evaluate the performance for the six regions measured in the office environment campaign (see Chapter 4)

a Bayesian M-ary hypothesis test [22] has to be used. $\hat{m}$ denotes the estimated region, π_i are the a priori probabilities given by $1/M$ which assumes each region is equally likely to transmit. For the M-ary hypothesis test we consider K multiple independent observations.

$$\hat{m} = \underset{m=1...6}{\arg\max}\ \pi_m p(\mathbf{y}|H_m) \tag{5.7}$$

We insert the probability densities of our regions and obtain (5.8).

$$\hat{m} = \underset{m=1...6}{\arg\max}\ \ln\left(\frac{\pi_m}{|\hat{\mathbf{\Sigma}}_m|^{K/2}}\right) - \sum_{k=1}^{K}(\mathbf{y}_k - \hat{\mu}_m)^H \hat{\mathbf{\Sigma}}_m^{-1}(\mathbf{y}_k - \hat{\mu}_m) \tag{5.8}$$

We evaluate (5.8) for different CIRs under test $\mathbf{y}$. By counting the right and wrong decisions we obtain the error probabilities for a certain tranmit region. $P\left(H_i|H_j\right)$ denotes the probability for the algorithm deciding for region i if region j is the transmit region.

The total error probability P_e is given by (5.9) and the average positioning error d_e for M regions is denoted in (5.9) [34]. d_{ij} is the distance error between region i and j. The distance of one region d_{ii} is calculated by $d_{ii} = \sqrt{2} \cdot W \cdot 10^{-2}$.

$$P_e = \sum_{j=1}^{M} \pi_j \sum_{i=1, i\neq j}^{M} P\left(H_i|H_j\right) \tag{5.9}$$

$$d_e = \sum_{j=1}^{M} \pi_j \sum_{i=1}^{M} P\left(H_i|H_j\right) d_{ij} \tag{5.10}$$

5.2 Performance evaluation

The goal of the performance evaluation is to gain error probabilities denoted as $P_e(\mathbf{y}|R)$ where R represents the transmitting region. The error probabilities shall be evaluated for different circumstances. This section investigates the performance in dependency of noise level, number of observations, amount of training data and region size.

The measurements were taken in the office environment with a high SNR level (around 56 dB). In order to simulate lower SNR points we corrupt our CIRs with additive complex Gaussian i.i.d. noise samples $\mathbf{n}$ with variance σ_n^2 as shown in (5.12). For each SNR point 10^3 noise realizations are generated. Afterwards the error probabilities are averaged over the realiazations. We use the SNR definition written in (5.11) where E_b is one due to energy normalization.

The covariance matrices are also corrupted by the same type of noise. This is done by adding the noise variance to the diagonal of the covariance matrix (5.13).

$$SNR = 10\log_{10}\left(\frac{E_b}{\sigma_n^2}\right) \tag{5.11}$$

$$\mathbf{y}_n = \mathbf{y} + \mathbf{n} \tag{5.12}$$

$$p(\mathbf{y}_n|R) = \mathcal{CN}\left(\hat{\mu}_R, \hat{\mathbf{\Sigma}}_R + \sigma_n\mathbf{I}\right) \tag{5.13}$$

We divide our W^2 CIRs into a set of training data to estimate the mean vector and the covariance matrix and test data to calculate the error probabilities using hypothesis testing. To perform this portioning we use K-fold cross validation [4]. To get statistically accurate results we averaged over 25 random divisions of training and test data.
For the evaluations in this chapter we assume zero mean. $0.3 \times W^2$ CIRs are used for the training phase and the rest for testing.

5.3 Results

Figure 5.1 and 5.2 show the performance of the exact, measured and artificial CIRs for the region pair $(3, 6)$ using the covariance approach. The exact CIRs are calculated from the geometry of the environment using ray tracing while the artificial CIRs are obtained from the reconstruction using the α and β estimation based on the Hough transform.
In both cases the performance of the CIRs generated using the Hough transform is slightly better than the performance using 3 CIRs for artificial CIR generation. $P_e(\mathbf{y}|3)$ and $P_e(\mathbf{y}|6)$ are not equal because our hypothesis test is an asymmetric decision problem. In Figure 5.2 the Hough transform approach reaches almost the same performance as the measured CIRs.
The fingerprints generated from the exact CIRs generated from tray tracing do not show feasible performance results. Too many paths are not covered by the ray tracing procedure and lead to wrong fingerprints.

The performance difference between between the COV and the PDP approach for two different region sizes is depicted in Figure 5.3 and Figure 5.4. As expected the COV approach performs better than the PDP approach because it takes also into account correlations between CIR taps.

Figure 5.5 shows the error probability depending on SNR using the COV approach assuming zero mean for a distant and an adjoining region pair. The Hough transform based approach was used in this figure for artificial CIR generation. As expected the neighboring region pair (1,2) performs worse than the distant region pair (3,6). Signatures from the distant region pair are better distinguishable.
We also notice the measured CIRs perform better than the artificially generated CIRs. For the neighboring region pair the performance difference between artificial and measured data is large. For 20 dB SNR we obtain 0.002 (meas.) vs. 0.07 (art.) for the misclassification error.

The performance considering all of the six regions is shown in the bar plots in Figure 5.6 to Figure 5.8. Region 3 is the transmit region, one observation is received. The probability deciding for region i if region 3 is transmitting is denoted as $P(H_i|H_3)$. In general the performance decreases if we increase the number of regions (hypothesis). Also in this setup the measured CIRs perform better than the artificial and artificial CIRs generated using the Hough approach perform slightly better than the CIRs generated using 3 measured CIRs. The regions near the transmit region show the highest probability for misclassification.

Table 5.1 contains the total error probability P_e and the total distance error d_e for measured and reconstructed CIRs with the Hough transform. It is worth to notice that increasing the number of observations increases the performance rapidly.

obs.	1	2	4
$P_{e,meas}$	0.1813	0.0093	0.0004
$P_{e,art}$	0.2131	0.1000	0.0081
$d_{e,meas}[m]$	0.1813	0.1331	0.1018
$d_{e,art}[m]$	1.1410	0.5986	0.1491

Table 5.1: Total error probabilities and distances with $W = 6$, $0.3 \times W^2$ Training samples and 20 dB SNR

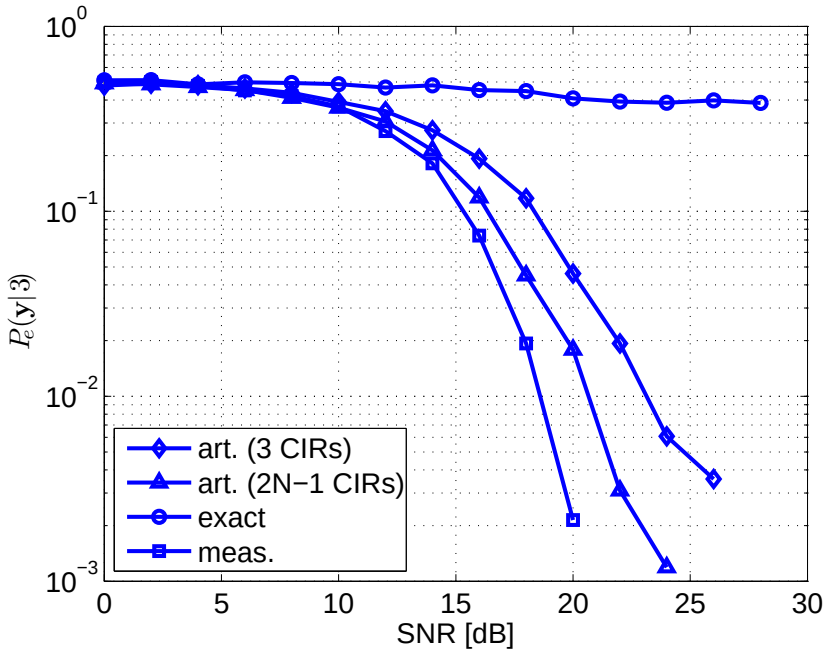

Figure 5.1: Error probability for region pair (3,6) with region 3 as transmit region, COV estimation, $W = 6$, $0.3 \times W^2$ training CIRs

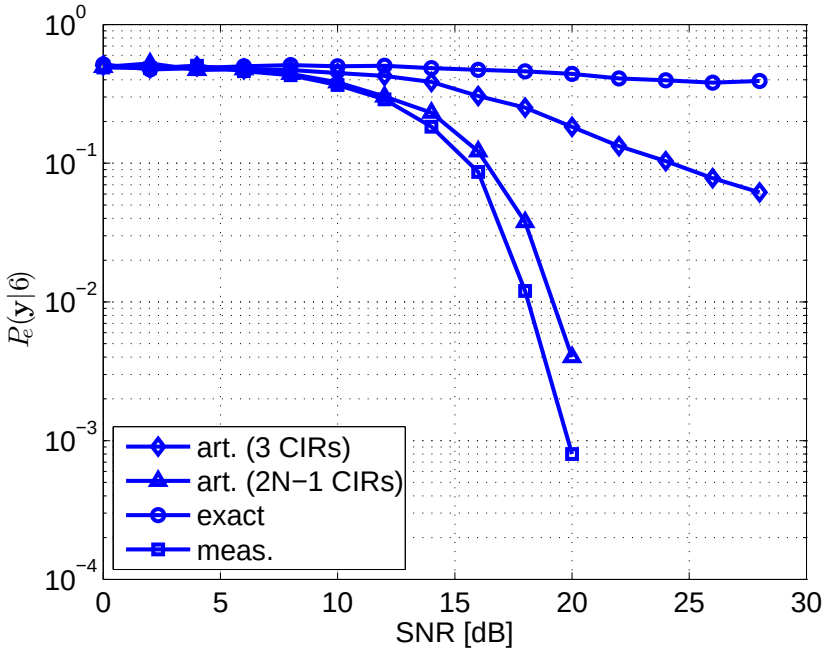

Figure 5.2: Error probability for region pair (3,6) with region 6 as transmit region, COV estimation, $W = 6$, $0.3 \times W^2$ training CIRs

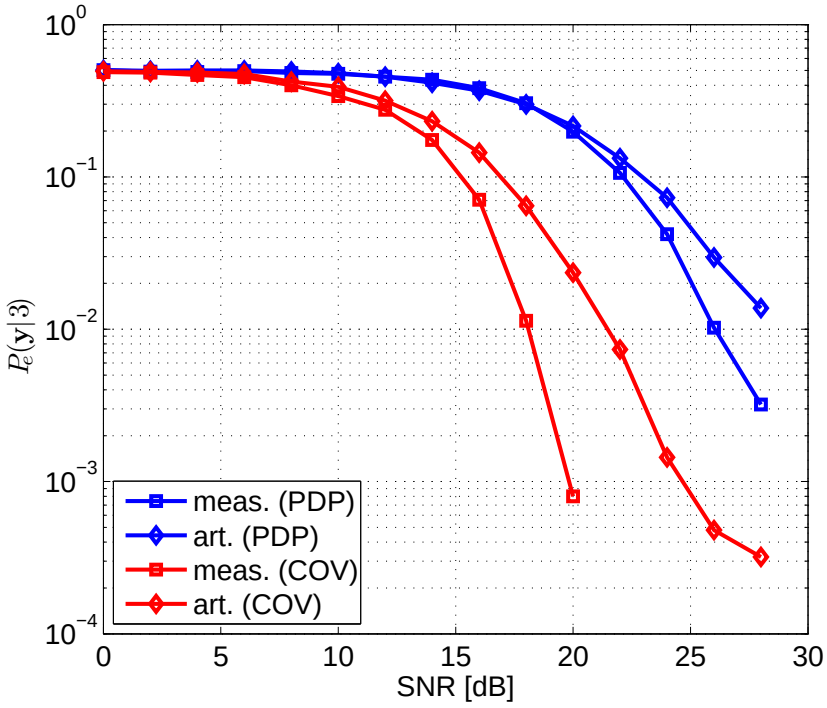

Figure 5.3: Error probability for region pair (3,6) for PDP and COV estimation, $W = 6$, $0.3 \times W^2$ training CIRs

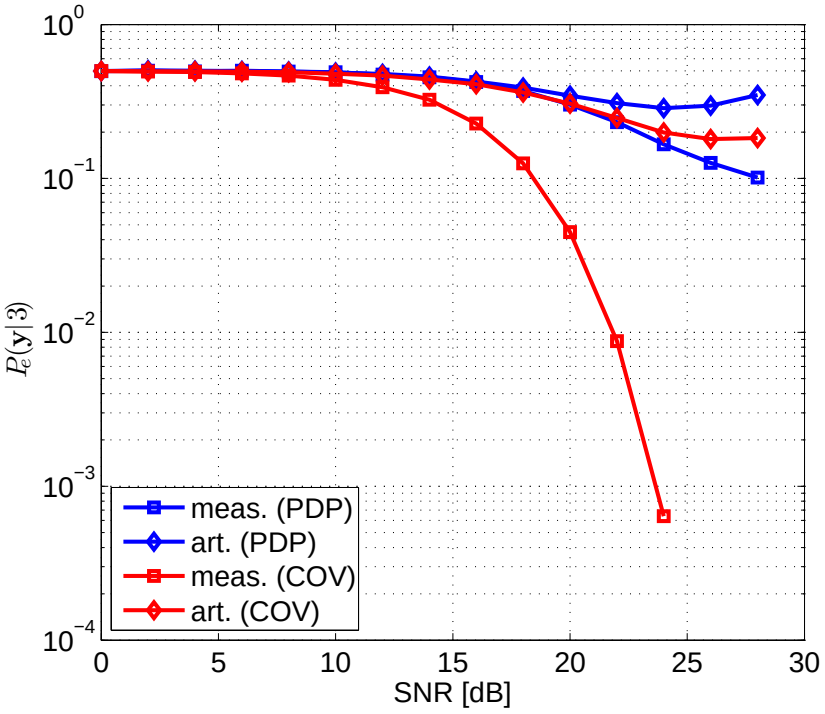

Figure 5.4: Error probability for region pair (3,6) for PDP and COV estimation, $W = 28$, $0.3 \times W^2$ training CIRs

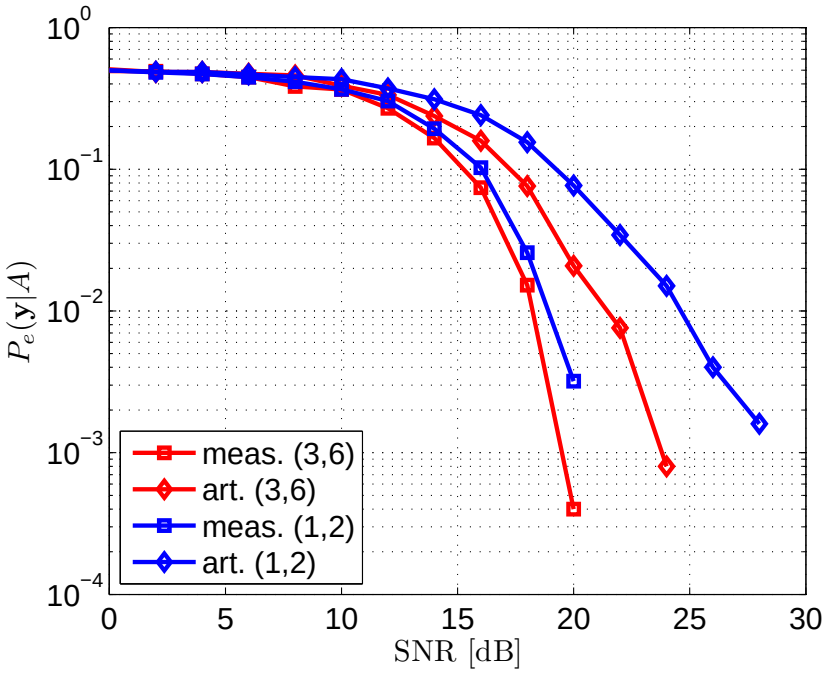

Figure 5.5: Error probability for region pair (1,2) and (3,6) with measured and art. generated CIRs, COV estimation, $W = 6$, $0.3 \times W^2$ training CIRs

5.3.1 Region Size

Let's consider the impact of the region size. While in Figure 5.8 a region with $W = 6$ the artificial CIRs reach an acceptable performance the error for misclassification is very high for regions with $W = 28$ in Figure 5.8.
This drawback can be compensated slightly using multiple observations. Using 4 independent observations increases the probability of right classification from around 30% to 45% in a region with $W = 28$ and from around 85% to almost 100% in a region with $W = 6$ as it is shown by Figure 5.9 and 5.8.
Lowering the region size increases the performance of the artificially generated CIRs. Figure 5.11 depicts that the artificial CIRs perform poorly for the region with $W = 28$ while the performance for regions with $W = 12$ and $W = 6$ is better.
For large regions the reconstruction of CIRs with our methods is not suitable anymore, because the variance of the path gains and delays over 28 cm in an indoor environment is too high. In small regions the variance is lower and the reconstruction works, which results in a lower misclassification error. It is possible small regions have the drawback to be not unique in the environment. Similar regions may occur in an indoor environment. Our measured regions are not sufficient to prove this assumption.

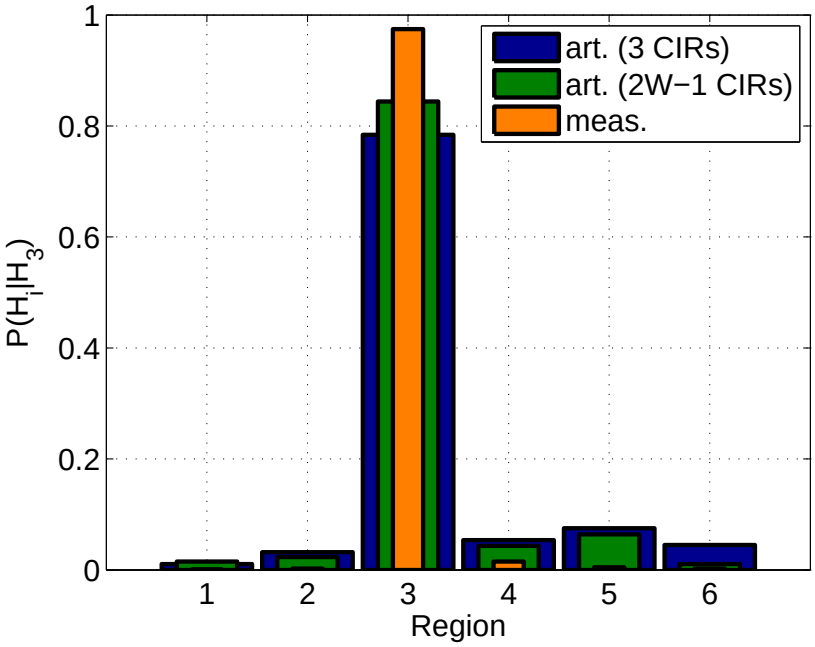

Figure 5.6: Error probability for all regions, region 3 is the transmit region, $W = 6$, $0.3 \times W^2$ training CIRs

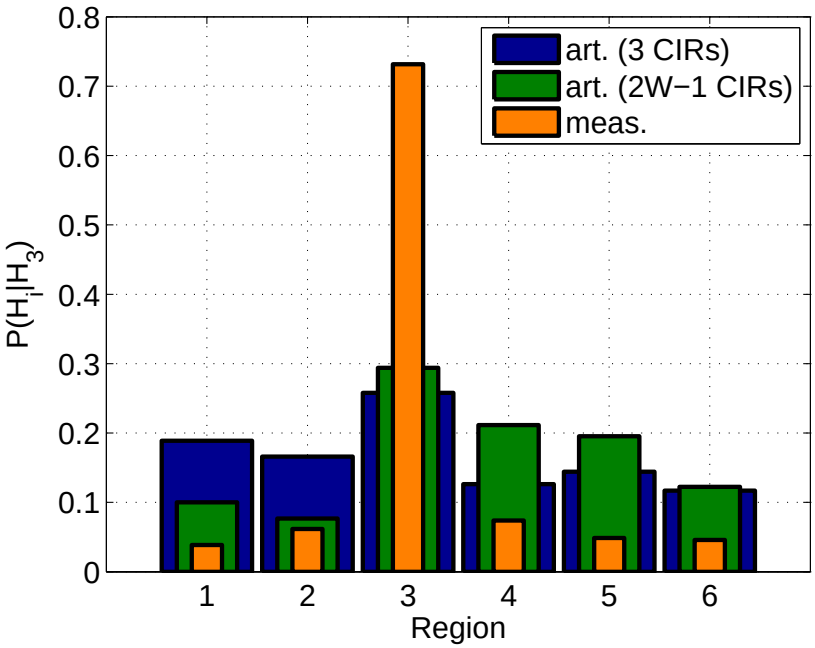

Figure 5.7: Error probability for all regions, region 3 is the transmit region, $W = 28$, $0.3 \times W^2$ training CIRs

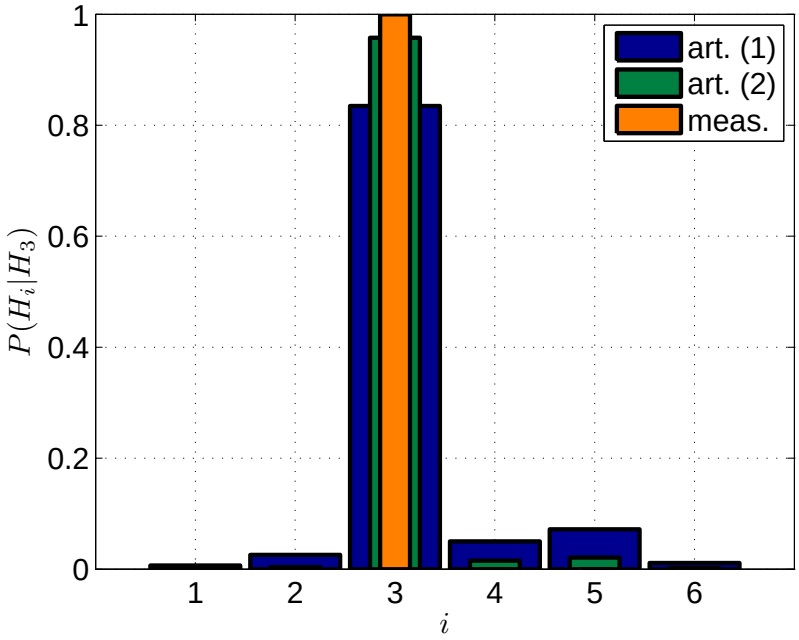

Figure 5.8: Error probability for all regions, region 3 is the transmit region, for multiple observations, $W = 6$, $0.3 \times W^2$ training CIRs

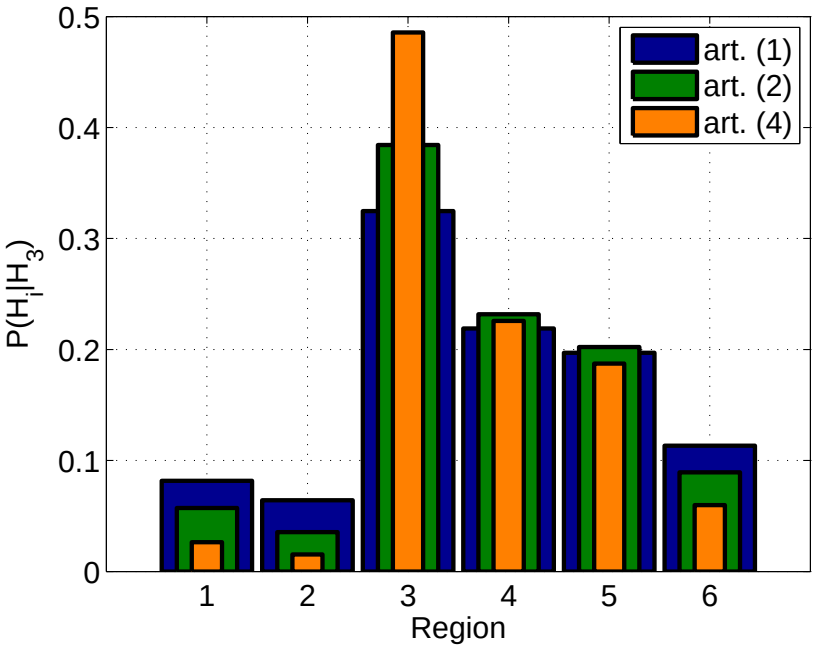

Figure 5.9: Error probability for all regions, region 3 is the transmit region, for multiple observations, $W = 28$, $0.3 \times W^2$ training CIRs

5.3.2 Number of training CIRs

Figure 5.10 shows the classification error over the amount of CIRs used for parameter estimation. The SNR value is set to 20 dB and the region width is 28. Small regions also require less training effort but show the same slope. The amount of a priori knowledge per region is an important parameter for location fingerprinting systems. A vast amount of a priori CIRs results in a large training phase.The main goal of this work was it to reduce the training phase.

The slope of the artificial CIRs is less steep than the slope of the measured CIRs because the temporal variation of the paths is lower.

For the NLOS regions the training phase is more exhaustive, because the temporal variation of the delays in the CIRs is higher than for LOS regions. This effect was already observed in [33].

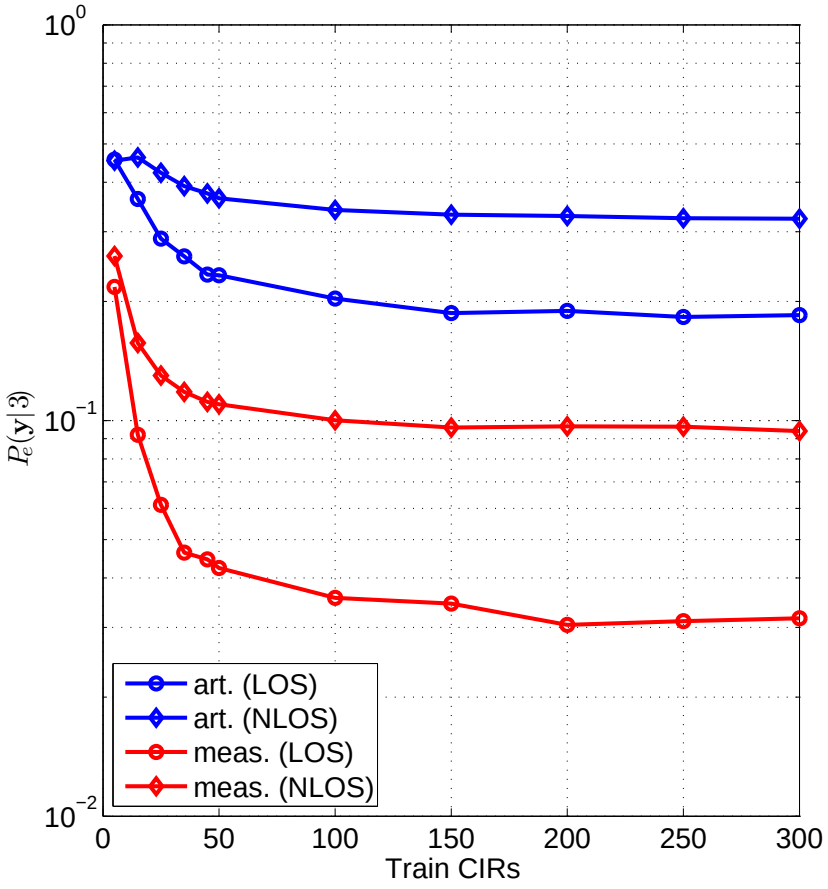

Figure 5.10: Error probability for region pair (3,6) with measured and art. generated CIRs over a priori knowledge

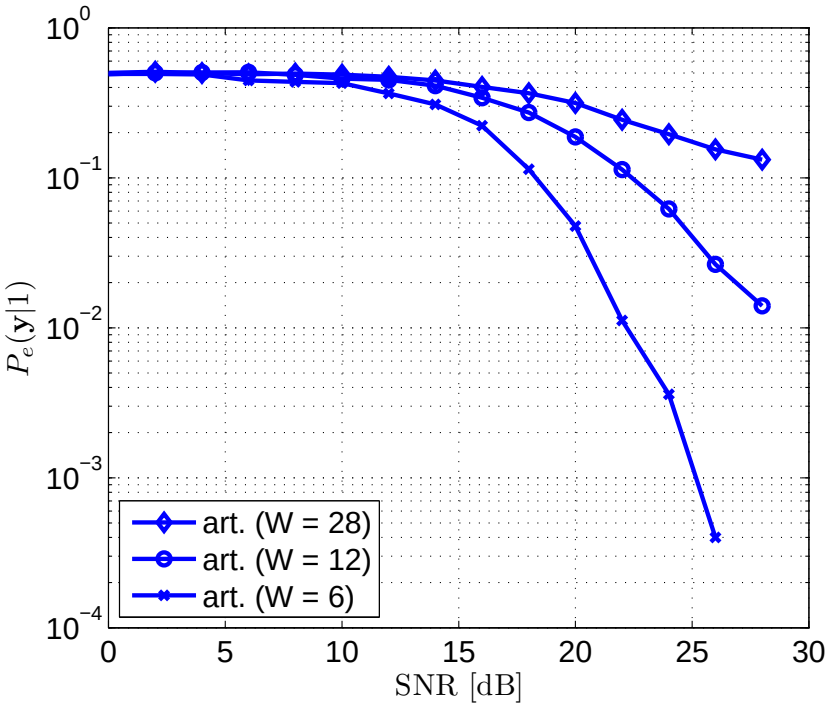

Figure 5.11: Error probability for region pair (1,2) with artificial and CIRs for different region sizes, $0.3 \times W^2$ training CIRs

5.4 Conclusion

The outcome of this chapter can be seen as the overall outcome of this work.
For UWB channel impulse responses with 4 GHz bandwidth from 2 GHz to 6 GHz and 125 channel taps we achieve a total distance error of 15 cm with the Hough based reconstruction method, 4 CIR observations an SNR level of 20 dB. The location positioning accuracy is acceptable for neighbor regions as well as for distant regions and non line of sight regions.
We reduced the number of measured training CIRs from $W^2 * 0.3$ to $2W - 1$ for the Hough based reconstruction and from $W^2 * 0.3$ to 3 CIRs with the simple reconstruction method. The larger the regions, the more training effort we save. But also the error of misclassification increases rapidly. In relation to the amount of saved training CIRs the reconstruction method with 3 measured CIRs is the most effective. The Hough based reconstruction gains slightly lower error probabilities but it is not worth the effort.
Fingerprints generated from ray tracing do not lead to usable results, even if for some paths of the CIRs match the ray tracing paths. There are too many paths not covered by the ray tracing. This leads to wrong estimates and the measured CIRs under test do not fit the probability models based on the CIRs obtained from ray tracing. Hence investigating the geometry of the environment is only helpful in an environment with deterministic paths like an anechoic chamber. Even putting additional reflectors in the environment did not help find traceable paths which coincide with the paths obtained from ray tracing. It was possible in some cases, but it mostly failed.
The number of estimated paths has an influence on the quality of reconstruction, but not on the performance evaluation. A possible explanation is that estimating 20 instead of 15 paths adds no paths which show significant changes in space to the artificial CIRs.
The most significant parameters for the location fingerprinting system are the region size and the number of independent observations.

A Parameter Estimation in an Artificial Propagagion Environment

A.1 Results

	l	LOS	1	2	3	4
$\tau_{x_0,y_0,l}$ [ns]	exact	7.5902	10.3736	16.3588	17.3478	20.4627
	est.	7.5877	10.3704	16.3593	17.3548	20.4907
	diff.	0.0025	0.0032	-0.00047	-0.007	-0.028
α_l	exact	-0.943	-0.687	0.988	-0.989	-0.347
	est.	-0.935	-0.681	0.995	-0.948	-0.410
	diff.	-0.008	-0.006	-0.006	-0.042	0.064
β_l	exact	-0.320	0.727	-0.148	-0.139	-0.936
	est.	-0.327	0.727	-0.151	-0.165	-0.898
	diff.	0.007	-0.001	0.003	0.025	-0.038

Table A.1: Results for reflection scenario with sinc pulses and an SNR of 30 dB

	l	LOS	1	2	3
$\tau_{x_0,y_0,l}$ [ns]	exact	7.5902	9.2571	12.2284	15.6196
	est.	7.5895	9.2559	12.2312	15.6184
	diff.	0.0007	0.0012	-0.0029	0.0012
α_l	exact	-0.943	-0.793	-1.000	-0.981
	est.	-0.941	-0.773	-0.961	-0.996
	diff.	-0.002	-0.020	-0.039	0.014
β_l	exact	-0.320	-0.596	-0.005	0.198
	est.	-0.308	-0.589	0	0.198
	diff.	-0.012	-0.007	-0.005	0

Table A.2: Results for scattering scenario with sinc pulses and an SNR of 30 dB

B Fingerprint generation from AEC measurements

B.1 Intensity plots

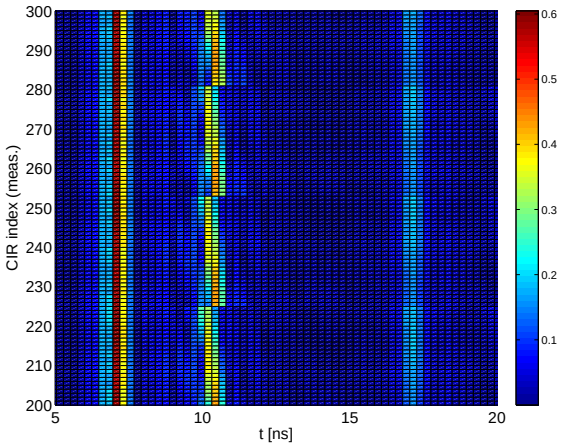

Figure B.1: 100 measured CIRs (absolute values) with simple alignment for Env. 1

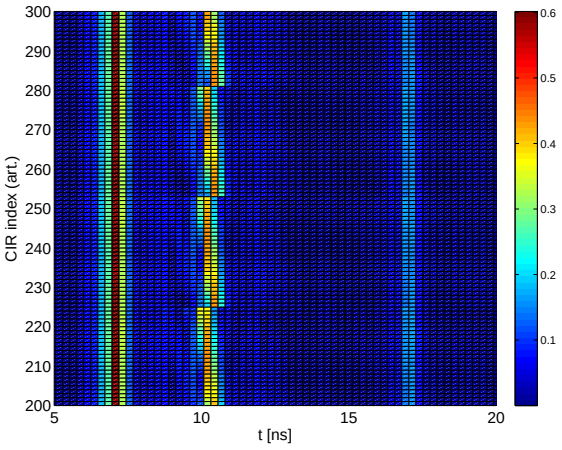

Figure B.2: 100 artificially generated CIRs (absolute values) with simple alignment for Env. 1

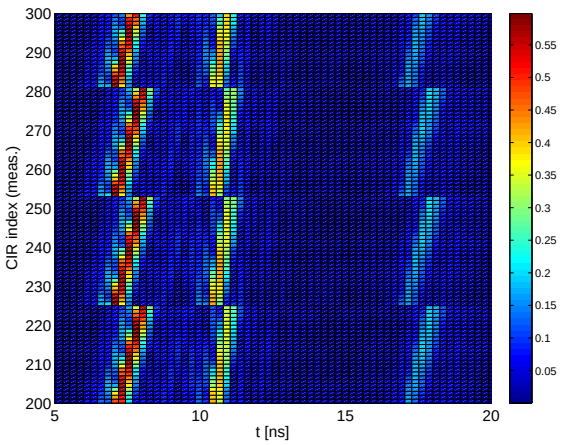

Figure B.3: 100 measured CIRs (absolute values) with extended alignment for Env. 1

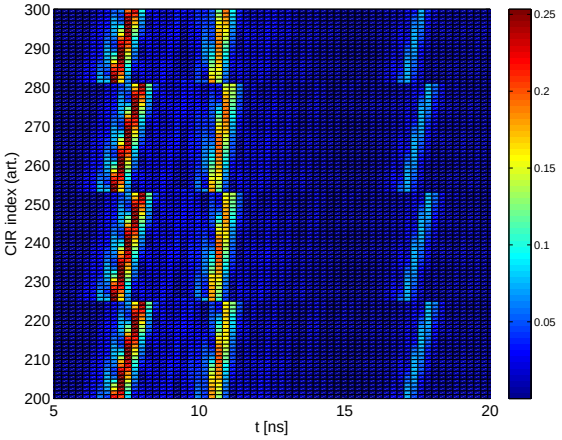

Figure B.4: 100 artificially generated CIRs (absolute values) with extended alignment for Env. 1

B.2 Covariance matrices

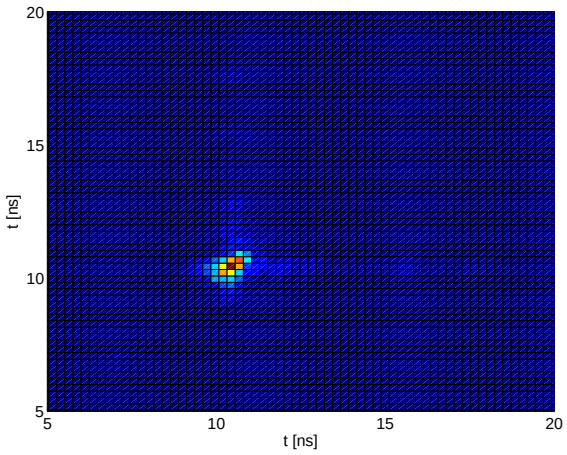

Figure B.5: Covariance Matrix of Env. 2, estimated from measured CIRs with simple alignment method

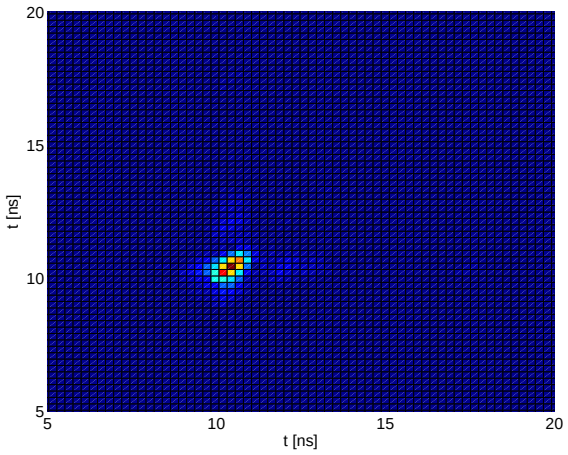

Figure B.6: Covariance Matrix of Env. 2, estimated from artificial CIRs with simple alignment method

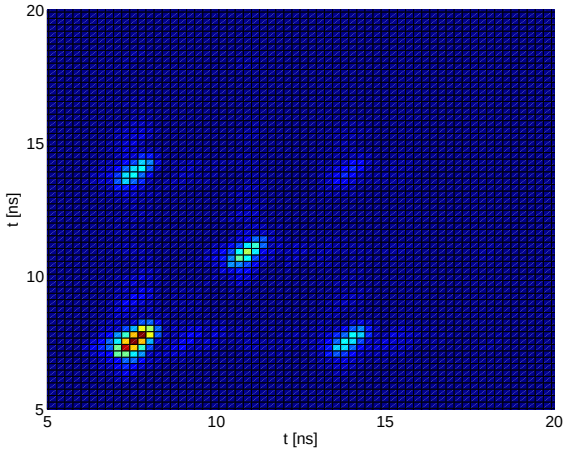

Figure B.7: Covariance Matrix of Env. 2, estimated from measured CIRs with extended alignment method

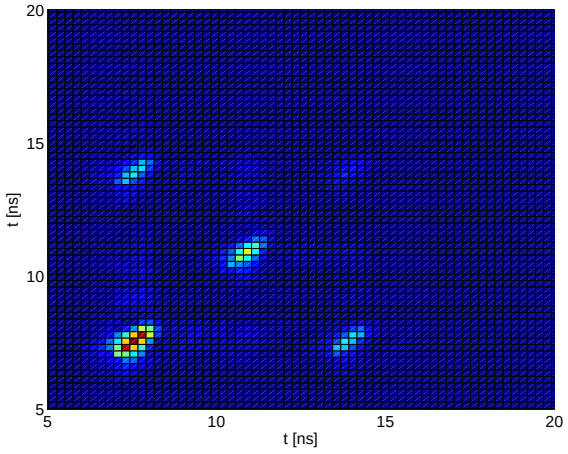

Figure B.8: Covariance Matrix of Env. 2, estimated from artificial CIRs with extended alignment method

C Fingerprint Generation from Office Environment Measurements

C.1 Mean vectors and covariance matrices

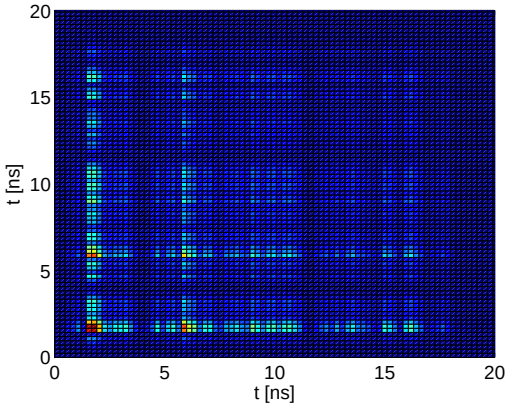

Figure C.1: Covariance Matrix of region 3, estimated from measured CIRs, $W = 6$, simple reconstruction method

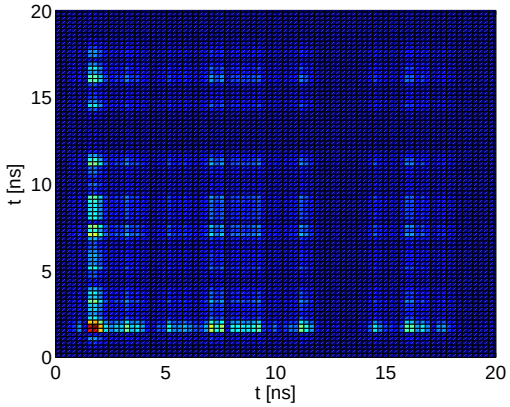

Figure C.2: Covariance Matrix of region 3, estimated from measured CIRs, $W = 28$, simple reconstruction method

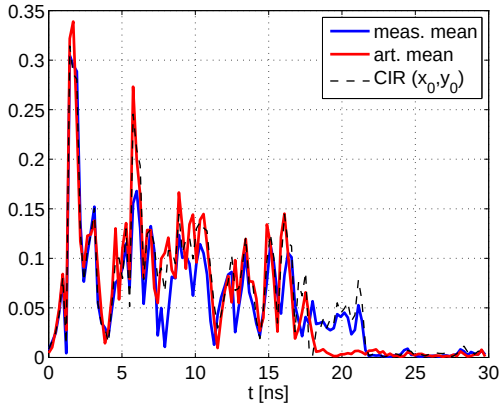

Figure C.3: Mean vectors for region 3, $W = 28$, simple reconstruction method

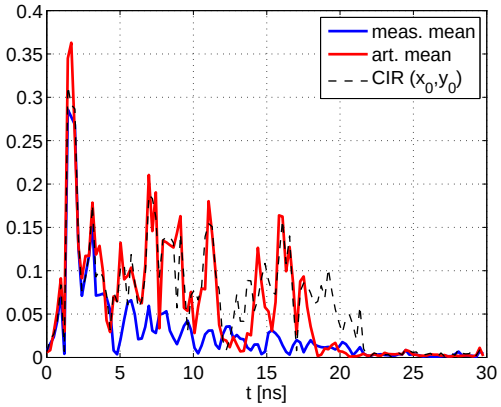

Figure C.4: Mean vectors for region 3, $W = 28$, simple reconstruction method

C.2 Fotos

Figure C.5: Picture of the office environment campaign using reflectors

Figure C.6: Picture of the office environment campaign using reflectors for a NLOS situation

Bibliography

[1] Ubisense AG. Ubisense. [online], 2010. http://www.ubisense.net.

[2] Frank Althaus, Florian Trösch, and Armin Wittneben. Geo-regioning in UWB networks. In *14th IST Mobile and Wireless Communications Summit 2005*, June 2005.

[3] Paramvir Bahl, , Paramvir Bahl, and Venkata N. Padmanabhan. Radar: An in-building rf-based user location and tracking system. pages 775–784, 2000.

[4] Christopher M. Bishop. *Neural Networks for Pattern Recognition*. Clarendon Press, Oxford, UK, 1995.

[5] P.L. Chin Cheong. Multipath component estimation for indoor radio channels. volume 2, pages 1177 –1181 vol.2, Nov 1996.

[6] Zebra Technologies Corporation. Zebra enterprise solutions. [online], 2010. http://zes.zebra.com.

[7] Scholtz R.A. Win M.Z. Cramer, R.J.-M. Evaluation of an ultra-wide-band propagation channel. *Antennas and Propagation, IEEE Transactions on*, 50(5):561 –570, May 2002.

[8] D.C. Daly, P.P. Mercier, M. Bhardwaj, A.L. Stone, Z.N. Aldworth, T.L. Daniel, J. Voldman, J.G. Hildebrand, and A.P. Chandrakasan. A pulsed uwb receiver soc for insect motion control. *Solid-State Circuits, IEEE Journal of*, 45(1):153 –166, jan. 2010.

[9] A. P. Dempster, N. M. Laird, and D. B. Rubin. Maximum likelihood from incomplete data via the em algorithm. *JOURNAL OF THE ROYAL STATISTICAL SOCIETY, SERIES B*, 39(1):1–38, 1977.

[10] Richard O. Duda and Peter E. Hart. Use of the hough transformation to detect lines and curves in pictures. *Commun. ACM*, 15(1):11–15, 1972.

[11] Tschudin M. Heddergott R. Dahlhaus D.-Ingeman Pedersen K. Fleury, B.H. Channel parameter estimation in mobile radio environments using the sage algorithm. *Selected Areas in Communications, IEEE Journal on*, 17(3):434 –450, Mar 1999.

[12] H.T. Friis. A note on a simple transmission formula. *Proceedings of the IRE*, 34(5):254 – 256, may 1946.

[13] Takada J.-I. Haneda, K. An application of sage algorithm for uwb propagation channel estimation. pages 483 – 487, Nov. 2003.

[14] Katharina Hausmair. UWB Radio Channel Analysis Using the SAGE Algorithm. Master's thesis, Signal Processing and Speech Communication Laboratory, Graz University of Technology, Austria, March 2010.

[15] Alereon Inc. Alereon ultrawideband solutions. [online], 2010. http://www.alereon.com.

[16] Ekahau Inc. Ekahau positioning engine. [online], 2010. http://www.ekahau.com.

[17] Tialinx Inc. Tialinx inc. [online], 2010. http://www.tialinx.com.

[18] Timedomain Inc. Plus ultra wideband real-time location system. [online], 2010. http://www.timedomain.com.

[19] Renbiao Wu Jian Li. An efficient algorithm for time delay estimation. *Signal Processing, IEEE Transactions on*, 46(8):2231 –2235, Aug 1998.

[20] R.A. Joon-Yong Lee, Scholtz. Ranging in a dense multipath environment using an uwb radio link. *Selected Areas in Communications, IEEE Journal on*, 20(9):1677 – 1683, Dec 2002.

[21] Kamol Kaemarungsi. *Design of indoor positioning systems based on location fingerprinting technique*. PhD thesis, Pittsburgh, PA, USA, 2005. Adviser-Krishnamurthy, Prashant.

[22] Steven M. Kay. *Fundamentals of statistical signal processing: detection theory*. Prentice-Hall, Inc., Upper Saddle River, NJ, USA, 1993.

[23] Steven M. Kay. *Fundamentals of statistical signal processing: estimation theory*. Prentice-Hall, Inc., Upper Saddle River, NJ, USA, 1993.

[24] Jian Li and P. Stoica. Efficient mixed-spectrum estimation with applications to target feature extraction. In *ASILOMAR '95: Proceedings of the 29th Asilomar Conference on Signals, Systems and Computers (2-Volume Set)*, page 428, Washington, DC, USA, 1995. IEEE Computer Society.

[25] Feng Wei Lichun Li, Chongsen Ran. Number of multipaths estimation by unitary transformation. volume 1, pages 98 – 102 Vol.1, June 2004.

[26] Fathy A.E. Kuhn M.J. Wang Y. Mahfouz, M.R. Recent trends and advances in uwb positioning. pages 1 –4, Sept. 2009.

[27] W. H. Press, S. A. Teukolsky, W. T. Vetterling, and B. P. Flannery. *Numerical recipes in C. The art of scientific computing*. Cambridge: University Press, second edition, 1992.

[28] Zheng-She Liu Renbiao Wu, Jian Li. Super resolution time delay estimation via mode-wrelax. *Aerospace and Electronic Systems, IEEE Transactions on*, 35(1):294 –307, Jan 1999.

[29] Thoma R.S. Richter, A. Joint maximum likelihood estimation of specular paths and distributed diffuse scattering. volume 1, pages 11 – 15 Vol. 1, May-1 June 2005.

[30] Florian Rtzer. Tragbare uwb-systeme, um durch mauern schauen zu knnen. online, 02 2010.

[31] Hayar A.M. Hofstetter-H. Aboutajdine D. Saadane, R. Statistical uwb channel model parameters estimation based on sage algorithm. pages 1195 –1199, Aug. 2007.

[32] Christoph Steiner. *Location Fingerprinting for Ultra-Wideband Systems*. Ph.d. thesis, ETH Zürich, 2010. to appear.

[33] Christoph Steiner, Frank Althaus, Florian Trösch, and Armin Wittneben. Ultra-wideband geo-regioning: A novel clustering and localization technique. *EURASIP Journal on Advances in Signal Processing, Special Issue on Signal Processing for Location Estimation and Tracking in Wireless Environments*, November 2007.

[34] Christoph Steiner and Armin Wittneben. Low complexity location fingerprinting with generalized UWB energy detection receivers. *IEEE Transactions on Signal Processing*, pages 1756–1767, March 2010.

[35] Sharman K.C. Stoica, P. Novel eigenanalysis method for direction estimation. *Radar and Signal Processing, IEE Proceedings F*, 137(1):19 –26, Feb 1990.

[36] Andreas F. Molisch Maria-Gabriella Di Benedetto Thomas Kaiser, Ian Oppermann. *UWB Communication Systems: A Comprehensive Overview*. Hindawi Publishing Publication, 2006.

[37] F. Troesch and A. Wittneben. Low power uwb transceivers for isi limited environments: Design and performance verification. pages 269 –273, sept. 2009.

[38] Zhang Naitong Wang Yang. A new multi-template clean algorithm for uwb channel impulse response characterization. pages 1 –4, Nov. 2006.

[39] Kailath T. Wax, M. Detection of signals by information theoretic criteria. *Acoustics, Speech and Signal Processing, IEEE Transactions on*, 33(2):387 – 392, Apr 1985.

[40] Wikipedia. Wireless usb — wikipedia, the free encyclopedia, 2010. [Online; accessed 5-March-2010].

[41] Klaus Witrisal, Geert Leus, Gerald J. M. Janssen, Marco Pausini, Florian Trösch, Thomas Zasowski, and Jac Romme. Noncoherent ultra-wideband systems: An overview of recent research activities. *IEEE Signal Processing Magazine*, July 2009.

[42] Cemin Zhang, M.J. Kuhn, B.C. Merkl, A.E. Fathy, and M.R. Mahfouz. Real-time noncoherent uwb positioning radar with millimeter range accuracy: Theory and experiment. *Microwave Theory and Techniques, IEEE Transactions on*, 58(1):9 –20, jan. 2010.

Deutsche Fassung:
Beschluss der Curricula-Kommission für Bachelor-, Master- und Diplomstudien vom 10.11.2008
Genehmigung des Senates am 1.12.2008

EIDESSTATTLICHE ERKLÄRUNG

Ich erkläre an Eides statt, dass ich die vorliegende Arbeit selbstständig verfasst, andere als die angegebenen Quellen/Hilfsmittel nicht benutzt, und die den benutzten Quellen wörtlich und inhaltlich entnommene Stellen als solche kenntlich gemacht habe.

Graz, am ……. ……..
(Unterschrift)

Englische Fassung:

STATUTORY DECLARATION

I declare that I have authored this thesis independently, that I have not used other than the declared sources / resources, and that I have explicitly marked all material which has been quoted either literally or by content from the used sources.

……. ……..
date (signature)